



12-2007

Deconvolution and Segmentation of Ground Penetrating Radar Images

Vincent Krause

Follow this and additional works at: https://scholarworks.wmich.edu/masters_theses



Part of the Electrical and Computer Engineering Commons

Recommended Citation

Krause, Vincent, "Deconvolution and Segmentation of Ground Penetrating Radar Images" (2007). *Master's Theses*. 4873.

https://scholarworks.wmich.edu/masters_theses/4873

This Masters Thesis-Open Access is brought to you for free and open access by the Graduate College at ScholarWorks at WMU. It has been accepted for inclusion in Master's Theses by an authorized administrator of ScholarWorks at WMU. For more information, please contact wmu-scholarworks@wmich.edu.



DECONVOLUTION AND SEGMENTATION OF GROUND PENETRATING
RADAR IMAGES

by

Vincent Krause

A Thesis
Submitted to the
Faculty of The Graduate College
in partial fulfillment of the
requirements for the
Degree of Master of Science
Department of Electrical and Computer Engineering

Western Michigan University
Kalamazoo, Michigan
December 2007

Copyright by
Vincent Krause
2007

ACKNOWLEDGMENTS

I wish to thank Prof. Ikhlas Abdel-Qader for her support and guidance through my graduate studies and research.

I am also grateful to the Department of Civil and Construction Engineering, especially Prof. Osama Abudayyeh, Prof. Sherif Yehia and Ammar Zalt for their technical support and for the use of their concrete.

Finally, I want to thank my mother and father for their encouragement and their patience.

Vincent Krause

DECONVOLUTION AND SEGMENTATION OF GROUND PENETRATING RADAR IMAGES

Vincent Krause, M.S.

Western Michigan University, 2007

Ground Penetrating Radar is a valuable tool for infrastructure condition evaluation as well as in archaeology and geology. The image produced by a GPR scan can be difficult to interpret due to the weak reflection amplitude, the overlap of reflections, and due to outside interference. This thesis proposes an algorithm to automate GPR scan interpretation. This will enable maintenance engineers to read GPR scans quickly and accurately.

The proposed algorithm framework uses an optimization-based deconvolution technique followed by a segmentation process. Each column of the image is deconvoluted and thus reducing them to a list of ordered pairs of reflection amplitude and delay time. The ordered pairs appearing in multiple columns are grouped to form an arc and line objects using a via similarity measures. The algorithm was successfully tested using synthetic and real GPR data.

TABLE OF CONTENTS

ACKNOWLEDGMENTS	ii
LIST OF FIGURES.....	v
CHAPTER	
I. INTRODUCTION.....	1
II. GPR OVERVIEW	3
Introduction to GPR	3
A-Scan	4
Light Traveling Through Media	4
Radar Paths.....	7
Convolutional Model of Radar Signal.....	8
Ambiguity in GPR A-Scans	9
B-Scan	9
Simulated GPR Scan of Layers	10
Simulated GPR Scan of Objects.....	15
GPR and Road Evaluation.....	18
III. INTERPRETATION OF GPR DATA.....	22
Human Analysis	22
Gain Boosting.....	22
Fourier Transform – F-k Filtering	24
Automated Methods for Object Detection	27

Table of Contents—continued

CHAPTER

Deconvolution	27
Fourier Methods	28
FIR Filter Methods	29
Blind Source Separation.....	29
Optimization Methods.....	30
IV. OPTIMIZATION-BASED DECONVOLUTION AND SEGMENTATION ALGORITHM.....	31
Deconvolution	31
Segmentation	39
V. EXPERIMENTAL RESULTS.....	41
Simulated GPR Data	41
Real GPR Data	48
VI. CONCLUSION.....	59
BIBLIOGRAPHY	61

LIST OF FIGURES

2-1: Reflection and Refraction of Light at Boundary	6
2-2: Model of GPR Scan of Parallel Layers.....	10
2-3: Simulated A-Scan of Parallel Layers.....	11
2-4: Deconvolution of A-Scan	12
2-5: Simulated B-Scan of Parallel Layers	14
2-6: Reflection Paths in a Simulated GPR Scan of Rebar Embedded in Concrete.....	15
2-7: Simulated B-Scan of Rebar Embedded in Concrete.....	16
2-8: Simulated A-Scan at Position 67 of Rebar Embedded in Concrete	17
2-9: Position 67 Within the Simulated B-Scan.....	17
2-10: Simulated B-Scan of Layer Defect	20
2-11: Simulated B-Scan of Object Defect.....	20
2-12: Simulated B-Scan of 'Invisible' Defect.....	21
3-1: Scan of 6-Inch Slab Without Gain Boosting	23
3-2: Scan of 6-Inch Slab With Gain Boosting	23
3-3: Scan of 4-Inch Slab.....	26
3-4: Transform of B-Scan of 4-Inch Slab	26
4-1: Flowchart of Deconvolution Algorithm	34
4-2: Deconvolution Error in a Simulated A-Scan.....	36
4-3: Correction of Deconvolution Error in a Simulated A-Scan	37

List of Figures - Continued

4-4: Flowchart of Sharpening Algorithm.....	38
5-1: Simulated Ground Response	42
5-2: Simulated A-Scan.....	42
5-3: Deconvoluted Ground Response of A-Scan.....	42
5-4: Reconstruction of A-Scan Using Deconvoluted Ground Response.....	43
5-5: Simulated A-Scan with Added Noise.....	43
5-6: Deconvoluted Ground Response of A-Scan with Added Noise.....	43
5-7: Reconstruction of Noise Free A-Scan Using Deconvoluted Ground Response	44
5-8: Simulated Ground Response of Crossing Lines with Same Polarity	45
5-9: Deconvoluted Ground Response of Crossing Lines with Same Polarity ...	45
5-10: Simulated Ground Response of Crossing Lines with Opposite Polarity	45
5-11: Deconvoluted Ground Response of Crossing Lines with Opposite Polarity.....	46
5-12: Simulated Ground Response of Concrete with Embedded Rebar	47
5-13: Simulated B-Scan of Concrete with Embedded Rebar.....	47
5-14: Deconvoluted Ground Response of Simulated B-Scan.....	47
5-15: Deconvoluted and Segmented Ground Response of Simulated B-Scan.....	48

CHAPTER I

INTRODUCTION

Ground Penetrating Radar is a useful method of performing non-destructive evaluation of roads, bridge decks and other underground structures. The data received from GPR scans is often complex and difficult to interpret. Part of the complexity is because the data is a convolutive mixture of the target's reflective properties and the characteristics of the transceiver.

Roads and bridge decks are subject to wear over time. Periodic assessment of these structures is crucial to their maintenance. Non-destructive testing methods allow road crews to detect defects while they are still small, before the integrity of roads and bridge decks are compromised. It is far cheaper to fix defects detected at an early stage than it is to wait for crises and failures in these structures.

One valuable method of non-destructive evaluation is ground penetrating radar. GPR reveals the structural composition of roads and bridge decks. GPR can locate damaged and deteriorated areas in roads and bridge decks, and determine the depth and properties of defects. In some cases, GPR scans can be performed without closing roads to traffic.

A disadvantage of GPR is that the data can be hard to interpret. The received data is a convolution of the physical properties of the underground structure with the properties of the antenna. The reflections of the radar pulse from underground features

often overlaps, and the interference due to this overlap may obscure details that construction engineers seek.

The algorithm proposed in this thesis reduces the complexity of GPR scans by removing the transceiver's characteristic pulse from the GPR data. The first stage of the algorithm deconvolutes each column of the GPR data through an iterative decomposition method using correlation to locate the position of each target reflection. The second stage segments the deconvoluted image, converting it to a database of points and arcs. Objects matching chosen criteria can be highlighted, removed, or added to the final image. The final image is ready for human experts and for automated systems to evaluate.

Chapter One presents the motivation and goals of this research. Chapter Two presents an overview of the theory and practice of GPR. Chapter Three presents methods commonly used in the interpretation of GPR data. Chapter Four presents the proposed deconvolution and segmentation algorithm. Chapter Five presents the results of applying the proposed algorithm to simulated and real GPR data. Chapter Six presents conclusions and future directions for research.

CHAPTER II

GPR OVERVIEW

Introduction to GPR

Ground penetrating radar is a method for evaluating underground structure. Simply put, it is radar aimed at the ground. A radar system is comprised of a transmitter which radiates an electromagnetic pulse into the target and a receiver which detects and records electromagnetic signals coming from the target. The transmitter and receiver may be placed at any position relative to each other and to the target[6,14], but the most common configuration is to mount the transmitting and receiving antennas onto a single transceiver unit.[7,11]

To perform a GPR scan at one location, the transceiver is positioned directly over the surface of the target. The distance between the transceiver and target varies depending on the type of antenna used. The transceiver is usually oriented so it is perpendicular to the surface of the target. This will direct aim the majority of the transmitted pulse into the target, and will minimize the reflections from other nearby objects. An electromagnetic pulse is transmitted, and electromagnetic signals are received and recorded for a short time.[11]

GPR scans are typically repeated multiple times on a target. A series of parallel lines are defined across the target's surface. The GPR transceiver is moved along these lines, taking scans at regular intervals of distance. The transceiver may be moved by

hand, mounted on a cart and pushed, or mounted on the back of a truck and driven over the target.

The data recorded in a GPR scan provides insight into the structures under the target's surface. This method allows the evaluation of the structure of a target without the destruction of the target.

GPR is currently used in geology[7], archeology[6], mining[37], for landmine detection and other military applications[5,10,26], and in civil engineering and construction. In civil engineering, it is used to evaluate roads[13], bridge decks[15], retaining walls[23], and other structures. Because GPR is non-destructive, these structures may be evaluated without drilling core samples and damaging good structures.[28]

A-Scan

An A-scan is a GPR scan taken at a single location.[14] An electromagnetic pulse is transmitted into the target surface. The pulse penetrates the surface, interacts with buried objects and layers, and is reflected back to the receiver. The data from an A-scan is represented by a column vector, and is plotted in a two-dimensional graph.

Light Traveling Through Media

An electromagnetic pulse is emitted by the GPR transceiver and the pulse radiates into the surrounding medium. The velocity of the pulse is the speed of light in the medium. The speed of light is determined by the refractive index of the medium, η .

$$\eta = \sqrt{\epsilon\mu} \quad 1$$

where ϵ is the dielectric constant and μ is the magnetic permeability. ϵ and μ are properties of how a material interacts with electric and magnetic fields. For the frequencies used by the GPR equipment and the materials being evaluated, we may treat $\mu \approx 1$. [28] The refractive index may be estimated as

$$\eta \approx \sqrt{\epsilon} \quad 2$$

The speed of light in a medium with refractive index η is

$$v = \frac{c}{\sqrt{\epsilon}} = \frac{c}{\eta} \quad 3$$

Given the time it takes a pulse to travel one way through a layer of material with refractive index η , the thickness of the layer can be calculated.

$$d = \frac{tc}{\eta} \quad 4$$

When the pulse reaches the boundary between two media, part of the pulse is reflected and part is transmitted. The amplitudes of the two new beams are functions of the refractive indices of the two media. Given a boundary between a medium whose refractive index is η_1 and one whose refractive index is η_2 , the coefficient of reflection Γ_{12} between two layers is

$$\Gamma_{12} = \frac{\eta_1 - \eta_2}{\eta_1 + \eta_2} \quad 5$$

and the coefficient of transmission T_{12} is

$$T_{12} = \frac{2\eta_2}{\eta_1 + \eta_2} \quad 6$$

Note that $T_{12} + \Gamma_{12} = 1$.

The angles of reflection and transmission beams at a boundary are also functions of the refractive indices of the two media. They are governed by Snell's Laws. If the beam enters with an angle of incidence θ_i , the angle of reflection θ_R is

$$\theta_R = -\theta_i \quad 7$$

and the angle of refraction θ_T is

$$\eta_1 \sin(\theta_i) = \eta_2 \sin(\theta_T) \quad 8$$

Note that the coefficients T_{12} and Γ_{12} affect the amplitudes of the two beams, and angles θ_R and θ_T affect the path. These terms do not directly affect the time delay. Reflection and refraction are illustrated in Figure 2-1.

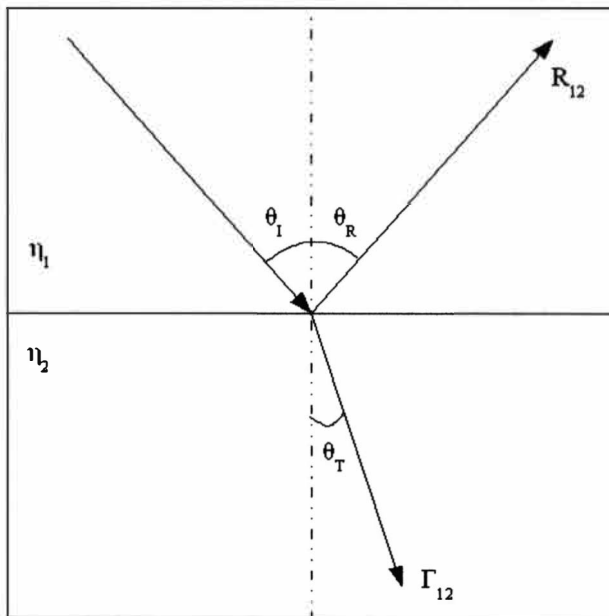


Figure 2-1: Reflection and Refraction of Light at Boundary

The amplitude of a pulse is also reduced based on its total travel time.

Inhomogeneities in media like concrete and soil scatter portions of the pulse and attenuate the signal. For short time intervals, this effect is far smaller than that of reflection and transmission, and is often omitted from the model. This effect is usually represented by an exponential decay function based on travel time.

Radar Paths

The transmitted pulse penetrates the target, interacting with every layer and object, traveling along multiple paths. Only pulses whose paths return to the receiver are detected. The amplitude and time delay of a received pulse provides information on every layer the pulse passed through and every boundary it interacted with.

The most useful travel paths are two-way paths. In two-way paths, the pulse enters the media, strikes a surface normal to its direction, and is reflected backwards along its original path. Note that a two-way path may be at any angle relative to the target's surface. Two-way paths tend to produce strong signals because they have the exactly one reflection, which minimizes the number of terms reducing the amplitude. Two-way paths are a primary focus in civil engineering applications.

Another set of paths is called ringing. Ringing occurs when a pulse enters a layer, reflects multiple times from the top and bottom of the layer, and then returns to the receiver. Ringing tends to produce weak signals due to multiple reflections. Ringing usually appears as repeated pulses beneath two-way reflections.

A near infinite number of other travel paths are possible. These paths tend to be

much weaker due to multiple reflections and exponential decay due to long travel times.

Roads and bridge decks are typically built with parallel layers of asphalt, concrete and soil with intermittent supporting rebar. Because of this straightforward structure, civil engineers can model GPR scan data in terms of two-way and ringing travel paths. Targets of archeology and geology GPR scans often have much more irregular and curving structures, and produce more irregular travel paths.

Convolutional Model of Radar Signal

Given a transmitted pulse $p(t)$, we expect to detect the received signal $s(t)$

$$s(t) = \sum_{i=1}^I e^{\alpha_i} (\prod_j \Gamma_j) (\prod_k T_k) p(t - \sum_l \frac{\eta_l d_l}{c}) \quad 9$$

where I is the total number of pulses detected in a GPR A-scan.[25] Each received pulse corresponds to a reflection path that travels from transmitter to receiver. For each i^{th} detected pulse,

e^{α_i} is a factor representing the gradual dissipation of the pulse in the media

$\prod_j \Gamma_j$ is the product of all j reflections along the i^{th} path

$\prod_k T_k$ is the product of all k transmissions along the i^{th} path

$p(t - \sum_l \frac{\eta_l d_l}{c})$ is the pulse, delayed by the sum of the travel time through all l

layers along the i^{th} path. Given no prior knowledge of the target's structure, the received signal is reduced to

$$s(t) = \sum_i a_i p(t - b_i)$$

10

where a_i is the amplitude and b_i the time delay of the i^{th} received pulse.

Ambiguity in GPR A-Scans

A single A-scan gives no information regarding the direction of the path that a pulse has traveled. The time delay does indicate the distance of a reflective object from the GPR transceiver, but not the angle of the path. The object may be deeply buried directly below the transceiver, or shallowly buried to the side of the transceiver.

A second A-scan taken a short distance from the first will typically reflect off the same layers and objects as the first. The amplitudes of corresponding reflected pulses will be the same in both A-scans because they will have the same coefficients of reflection and transmission. Because of the different starting points, the angles of reflection, the path lengths, and the travel times in each A-scan will be different. A series of A-scans can show whether the transceiver is approaching, directly above, or moving away from an object. The angles of the reflective paths and shape of the reflective object can then be determined.

B-Scan

A B-scan is a series of GPR scans taken at multiple locations.[14] The locations are typically regular intervals along a straight line. The received data is represented by an $M \times N$ matrix where n represents the n^{th} scan location and m represents the m^{th} sampling time interval. Each column of a B-scan is an A-scan taken at the n^{th} location. The data

in a B-scan is typically presented as a grayscale image where negative values are black, positive values are white, and zero values are gray.

A series of reflections from a single underground object will appear as a band or arc on a B-scan. These arcs will appear as sets of white-black-white or black-white-black lines in the grayscale image of B-scan data. The shape of the arc provides information on the depth, position and shape of the reflective object.

Simulated GPR Scan of Layers

Many targets of GPR scans, such as roads and bridge decks, are made of parallel layers.[15] Figure 2-2 shows a simple model of a GPR scan of a target made of three layers.

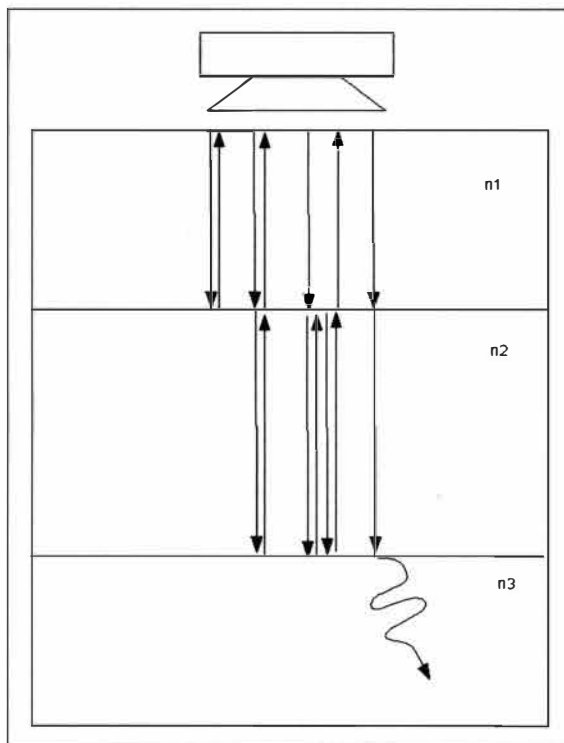


Figure 2-2: Model of GPR Scan of Parallel Layers

The reflections occur in the same space in reality; they are separated in this image for clarity. If the beam enters the target at an angle, its reflection at each layer will be away from the receiver, and the pulse will not be detected. The only pulses detected by the receiver are those that have an angle of incidence of 0° . The simulation shows three reflection paths: a reflection from the 1-2 boundary, a reflection from the 2-3 boundary, and ringing within the second layer. These reflections appear in the simulated A-scan of the target shown in Figure 2-3.[22,25] In this case, the A-scan can be deconvoluted graphically as shown in Figure 2-4.

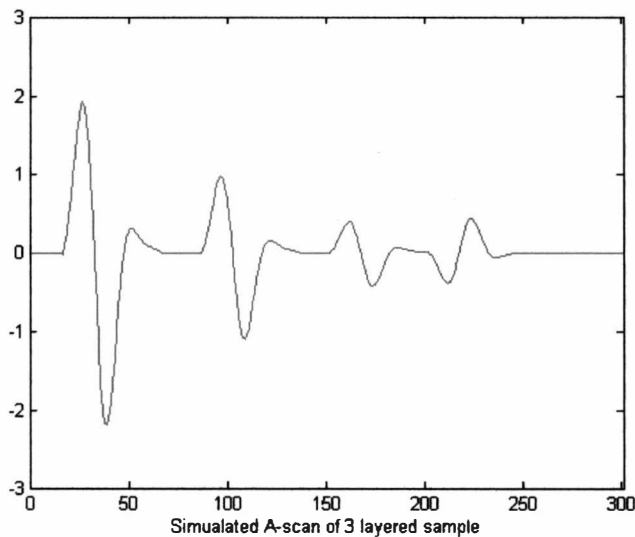


Figure 2-3: Simulated A-Scan of Parallel Layers

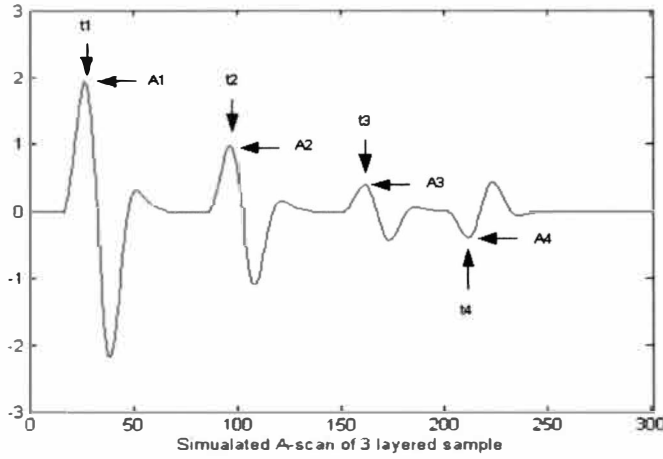


Figure 2-4: Visual Deconvolution of A-Scan

The first pulse is self-coupling, the receiver detecting the raw pulse directly from the transmitter.[11,21] The specifics of self-coupling depend on the transceiver being used. In some cases, this pulse may be superimposed with the first reflection from the air-surface boundary. In this simulation, the pulse is interpreted as occurring at t_1 with relative amplitude $A_1=1$.

The second pulse is the reflection from the 1-2 junction. The time delay is travel time from transmitter to the boundary plus travel time from the boundary to the receiver. Because both paths are the same, this is known as the two-way travel time through layer one.

$$t_2 = \frac{2d_1\eta_1}{c} + t_1$$

11

The amplitude of the pulse is reduced by the reflection coefficient Γ_{12}

$$A_2 = \Gamma_{12} = \frac{n_1 - n_2}{n_1 + n_2} \quad 12$$

If the refractive index η_1 of the top layer is known, the thickness of the top layer d_1 and the dielectric constant of the second layer η_2 can be calculated. An approximate value of η_1 is often chosen from a chart given the material of the top layer. For instance, if the top layer is concrete, we may look up that ϵ_1 is approximately 6 and that η_1 is approximately 2.45.

The third pulse is a reflection from the 2-3 junction. The time delay is the two way travel time through layer one and layer two.

$$t_3 = \frac{2d_1\eta_1}{c} + \frac{2d_2\eta_2}{c} + t_1 \quad 13$$

The amplitude A_3 is reduced by the interactions with each boundary it encounters: the transmission coefficient T_{12} , the reflection coefficient Γ_{23} , and the transmission coefficient T_{21} .

$$A_3 = T_{12}\Gamma_{23}T_{21} = \frac{2n_1}{n_1 + n_2} \frac{n_2 - n_3}{n_2 + n_3} \frac{2n_2}{n_1 + n_2} \quad 14$$

Given our estimated η_1 and calculated d_1 and η_2 , we can find d_2 and η_3 .

The fourth pulse is the result of ringing. Ringing occurs when a beam reflects multiple times, staying within a single layer. The amplitude A_4 is

$$A_4 = T_{12}\Gamma_{23}\Gamma_{21}\Gamma_{23}T_{21} = \frac{2n_1}{n_1 + n_2} \frac{n_2 - n_3}{n_2 + n_3} \frac{n_2 - n_1}{n_1 + n_2} \frac{n_2 - n_3}{n_2 + n_3} \frac{2n_2}{n_1 + n_2} \quad 15$$

and the time delay t_4

$$t_4 = \frac{2d_1\eta_1}{c} + 2\frac{2d_2\eta_2}{c} + t_1 \quad 16$$

In this simulation, layer three represents the substrate. There are no layers beneath to reflect the pulse back, and the third layer extends deeper than the pulse can penetrate. Any portion of the pulse that enters the third layer does not return to the receiver.

A B-scan is a series of A-scans taken at different locations. Because the layers in this model are parallel, the same signal should be received at every scan location. Therefore the B-scan should be made of parallel lines. A simulated B-scan is shown in Figure 2-5.

This is a theoretical example. In practice, the amplitudes decay exponentially with time, which makes calculating the refractive indices and thickness of layers difficult and inaccurate.

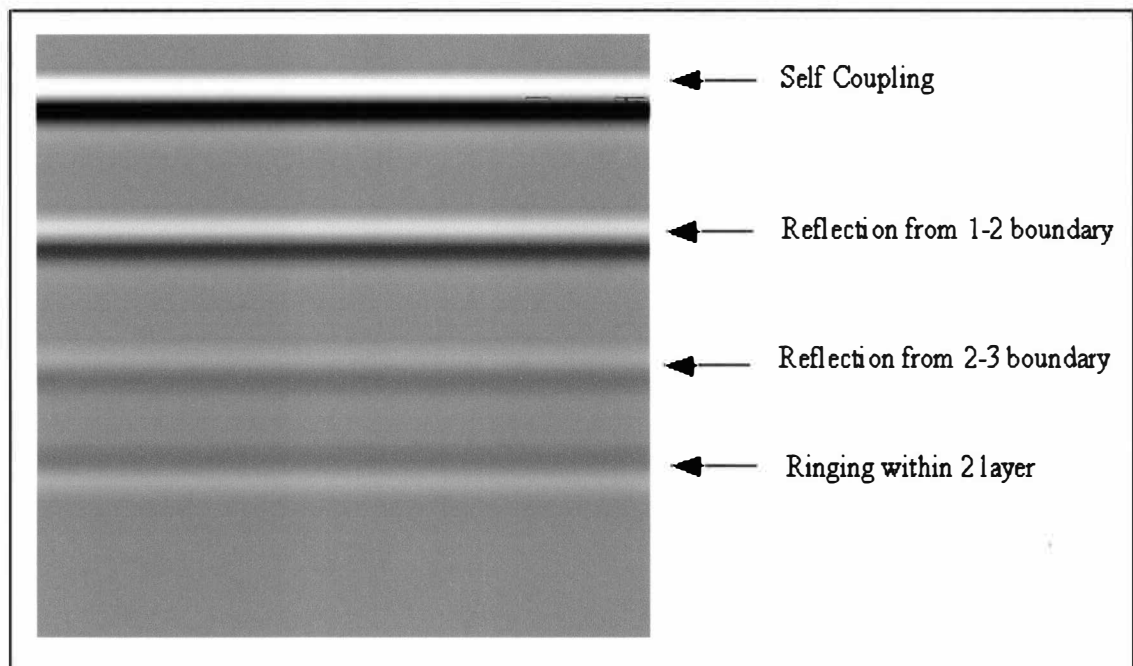


Figure 2-5: Simulated B-Scan of Parallel Layers

Simulated GPR Scan of Objects

Buried objects also reflect and refract electromagnetic pulses. The surface of an object is typically not parallel to the layers surrounding it. In order to have a transmitted pulse reflect off an object and return to the receiver, it must reflect off a region of the object that is normal to the direction of the pulse. The reflected pulse's two-way travel path may be at an angle relative to the surface. The shape of the reflection arc in a B-scan is dependent on the shape of the object. When the underground object has a simple geometry, it may be possible to predict the shape its reflection.[6,12] For example, a buried sphere or cylinder perpendicular to the scan direction will produce a hyperbolic arc in a B-scan.[3,8,18,33]

Figure 2-6 shows a simple model of rebar embedded in concrete.[15] In this model, the rebar are perpendicular to the path of the GPR scan.

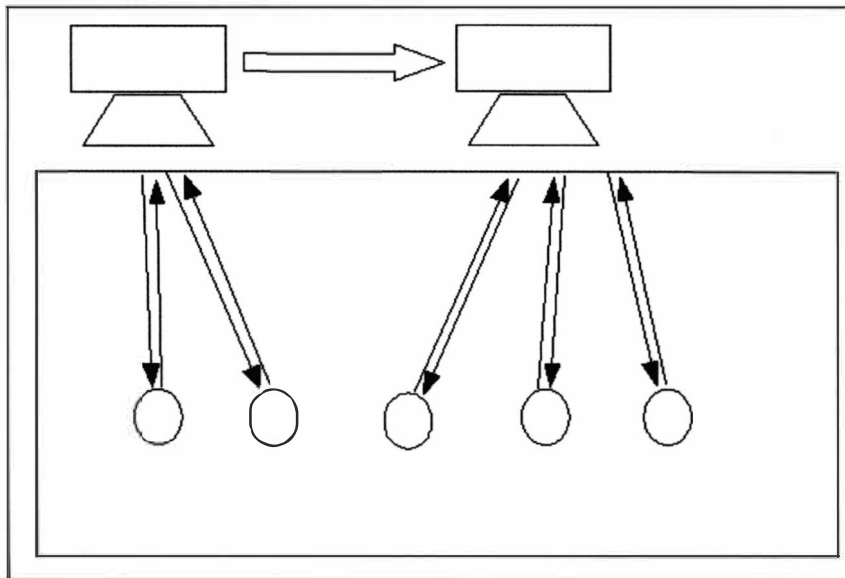


Figure 2-6: Reflection Paths in a Simulated GPR Scan of Rebar Embedded in Concrete

At each scan location, reflections from more than one rebar may be detected. As the transceiver approaches a rebar, the path distance and the travel time of the reflected pulse decrease. The travel time is minimized when the transceiver is directly above the rebar, and increases as the transceiver moves away. A simulated B-scan is shown in Figure 2-7.

The reflection from an object can appear in multiple A-scans, including when the transceiver is not directly above the object. Multiple embedded objects with similar reflective properties can create ambiguous reflections on an A-scan. The B-scan is needed to properly interpret specific pulses on a given A-scan. An example of this is shown in Figures 2-8 and 2-9.

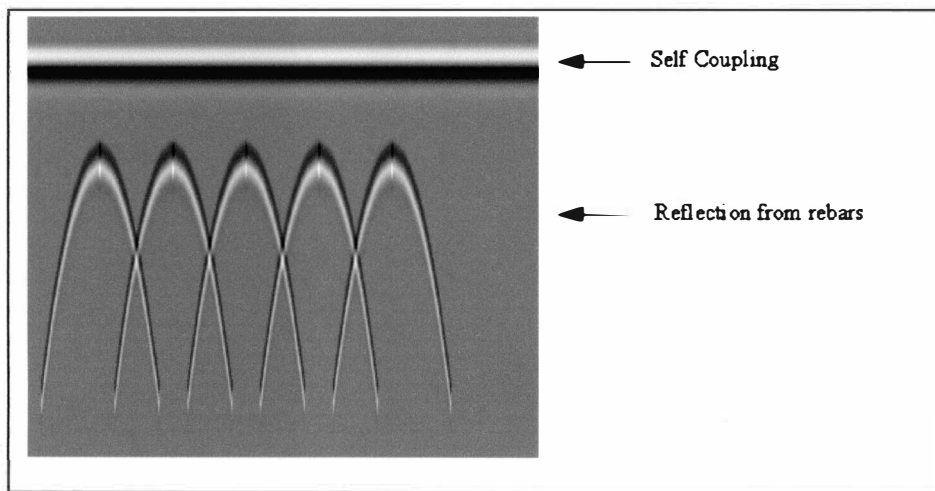


Figure 2-7: Simulated B-Scan of Rebar Embedded in Concrete

The A-scan in Figure 2-8 represents the 67th position of the simulated scan, taken from column 67 of the B-scan as shown in Figure 2-9. The first pulse is self-coupling, and the second and third pulses are reflections from embedded rebar. The time delay of

rebar reflection can be measured, but the A-scan gives no insight into the position of each rebar. Referring back to Figure 2-9, the B-scan shows that the first pulse is a member the left-most arc and the second is a member of the second arc.

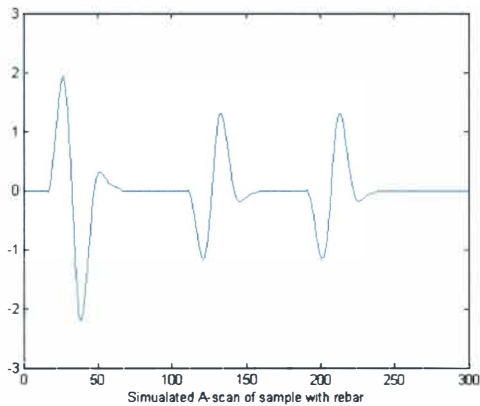


Figure 2-8: Simulated A-Scan at Position 67 of Rebar Embedded in Concrete

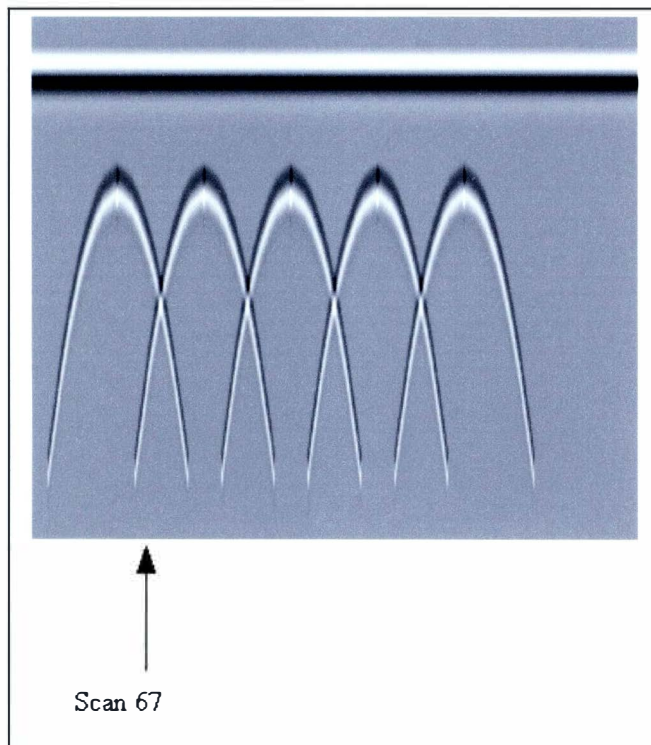


Figure 2-9: Position 67 Within the Simulated B-Scan

The relative amplitude of an object's reflection may be used to calculate the refractive index of the object. The process is the same as calculating for a layer.

The strongest reflection from an object is typically the two-way reflection path. Other paths are possible, including ringing, but these tend to be weaker.

GPR and Road Evaluation

Highway engineers use GPR to evaluate roads, bridge decks and other man made structures.[13] These structures become degraded over time due to heavy use, cycles of freezing and thawing, water penetration, erosion, etc. This degradation leads to the formation of defects, regions where the structure changes shape or changes properties.

The most important defects for road evaluation are delaminations and voids. Delaminations occur when the layers of the structure separate and the gap is penetrated by foreign materials. Voids occur when a layer is penetrated by foreign materials. The foreign material may be air, water, soil, or a corruption of the original building material. A defect will typically have a different refractive index than its surrounding material, and may be visible in a GPR scan.[11] Defects may appear as new layers, new objects, or as a distortion of the objects and layers below the defect.[23]

Figure 2-10 is a simulated B-scan of a delamination. The delamination may appear to be an additional layer that should not be present. In this case, the method for evaluating good layers can be applied to find the depth to and thickness of the defect. The refractive index may also be calculated, which will give insight to the type of defect.

Note that the presence of the defect alters the reflection from the layer below it.

Figure 2-11 is a simulated B-scan of a void with a rounded surface and an index of refraction very different than its surrounding material. The defect appears to be an object that should not be present. The reflection from an object-like defect will appear as a curve on the B-scan. As with other objects, this defect reflects along diagonal paths. It may be assumed that the center of the defect is located near the peak of its reflected arc on the B-scan. It is uncertain whether the lower arc is the lower edge of the defect or a refracted view of the lower layer's reflection.

Figure 2-12 is a simulated B-scan of a defect with an irregular surface or with an index of refraction similar to its surrounding material. Because of its properties, the defect does not return a strong reflection and is effectively “invisible”. This defect can be discovered by the distortion of expected reflections from layers below the defect. Note in the example that the reflections from the layers below the defect are distorted or missing. Depth and material type may not be determined in this case, but general position can be found.

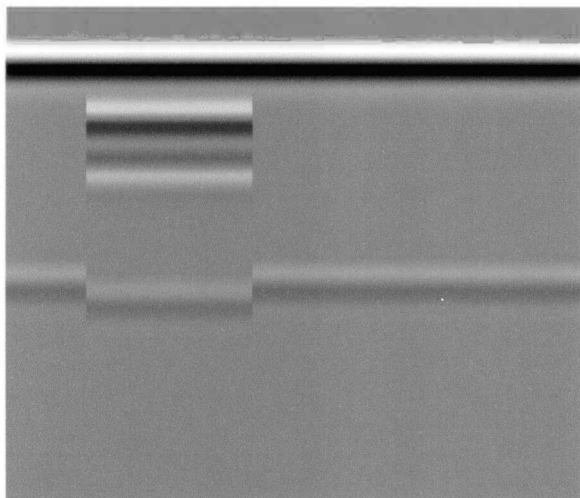


Figure 2-10: Simulated B-Scan of Layer Defect

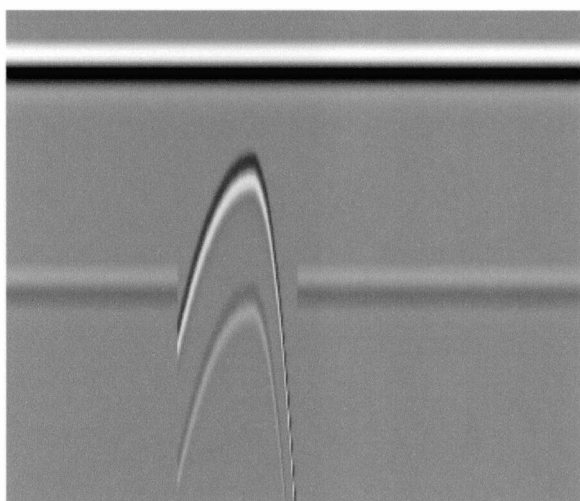


Figure 2-11: Simulated B-Scan of Object Defect

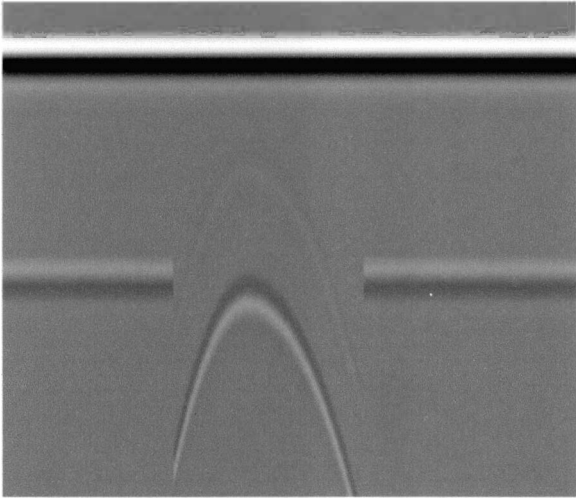


Figure 2-12: Simulated B-Scan of 'Invisible' Defect

CHAPTER III

INTERPRETATION OF GPR DATA

Human Analysis

GPR data can be visually evaluated by human experts. The GPR data is converted to an image where a pixel's particular shade of gray or color corresponds to the numerical value of its data point. The data is interpreted based on prior knowledge of the target, experience from evaluating other GPR scans and experience from creating simulations of GPR scans. Based on this experience, the expert detects objects and layers, the shape of and depth to objects, the type and quality of the surrounding media.

When performing visual inspection of GPR data, image processing techniques can be applied to the data.

Gain Boosting

The model of GPR convolution predicts that received GPR signals decay exponentially over time. It also predicts that received signals are diminished for every reflection and transmission in a pulse's reflection path. What tends to happen is that the strongest signal in a GPR scan is self-coupling, which has zero or one reflections and has the shortest time delay. Unfortunately, self-coupling is also the least interesting signal. Reflections from deep objects and layers tend to be much weaker.

In addition, low amplitude pulses in raw GPR data become subtle shades of gray when converted to an image. Many viewers find it hard to distinguish subtle changes in

shades of gray, as compared to shades of near-white.

Gain boosting is a method that remedies these problems.[1] The data in each column of the GPR data is multiplied by and added to by another equation. The new signal is of the form

$$s'(t) = e^{at} s(t) + g(t) \quad 17$$

where a is a constant and $g(t)$ is usually an exponential or hyperbolic sine function chosen by the user. The exponential term counters the exponential decay of the GPR signal over time. The $g(t)$ forces the average value of $s'(t)$ to near maximum for high values of t . This makes the lower region of the B-scan brighter than the upper region, and makes pulses easier to see.

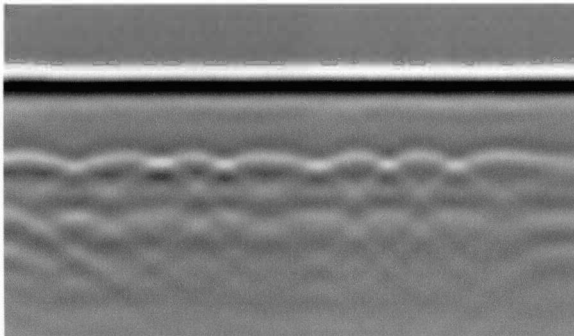


Figure 3-1: B-Scan of 6-Inch Slab Without Gain Boosting

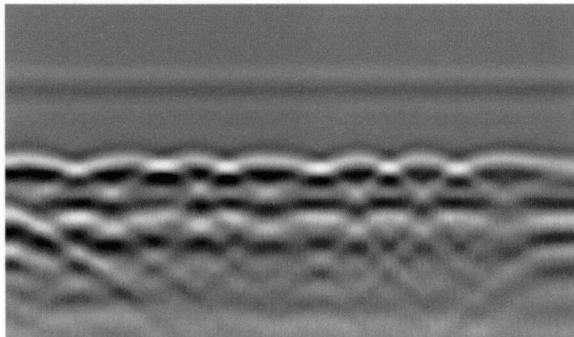


Figure 3-2: B-Scan of 6-Inch Slab With Gain Boosting

Figure 3-1 is the raw data of a GPR scan of an 8-inch test slab. Note that the self-coupling is the brightest feature in the image, and the reflections off of rebar are much fainter and harder to see. Figure 3-2 is the data after gain boosting, using the default settings on RADAN software. The self-coupling is greatly diminished, and the later reflections are much more prominent.

GPR scanners and analysis software allows the application of gain boosting with customized parameters to suit the application. While gain boosted data is visually appealing, it may not be suitable for mathematical analysis. For example, gain boosting will keep the time delay of a particular reflection constant but will change its amplitude and pulse shape.

Fourier Transform - F-k Filtering

The Fourier transform can be applied to GPR data in one or two dimensions.[1] When applied by column, the Fourier transform may be used to remove noise from outside sources. A band-pass filter may be constructed to pass frequencies found in the transmitter's pulse and block outside frequencies.[21] When applied by row, the Fourier transform may be used to remove low frequency and constants. This may be used to remove horizontal layers from the data. In practice, these functions are usually performed using image filters in the time-space domain and not in the Fourier domain.

When the Fourier transform is applied to the two-dimensional matrix of GPR data, it is called F-k filtering or migration[11,12]. The axes of a matrix of GPR data correspond to position in the X dimension and time in the Y dimension. When the matrix

is converted using the two-dimensional Fourier transform, the X dimension becomes the wavenumber k (the number of wavelengths per unit length), and the Y becomes frequency f . Filters that operate on this transformed data are known as F-k filters. F-k filters are used to remove repeated and angled components from the image. It is used primarily to remove diagonal arcs from GPR data, but has been applied to object detection.[30,34]

Reflections from objects tend to have a horizontal region when the transceiver is directly above the object and diagonal arcs as the transceiver moves away. The long diagonals of these arcs may obscure deeper reflections. In many cases, it is desirable to remove the diagonals and keep the horizontal regions.

In F-k filtering, the Fourier transform is applied to the two dimensional matrix of GPR data. Figure 3-3 shows a GPR scan, and Figure 3-4 shows the absolute values of the Fourier transform of that scan in a grayscale image. In the converted data there will be prominent diagonal components. An opaque filter to these regions, setting their values of the diagonal components to zero. The inverse Fourier transform is applied to the filtered image, and the resultant image should be a series of horizontal bands with the diagonal arcs removed.

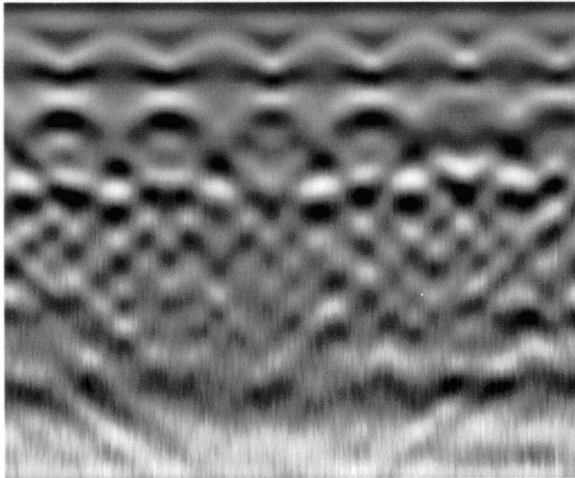


Figure 3-3: B-Scan of 4-Inch Slab

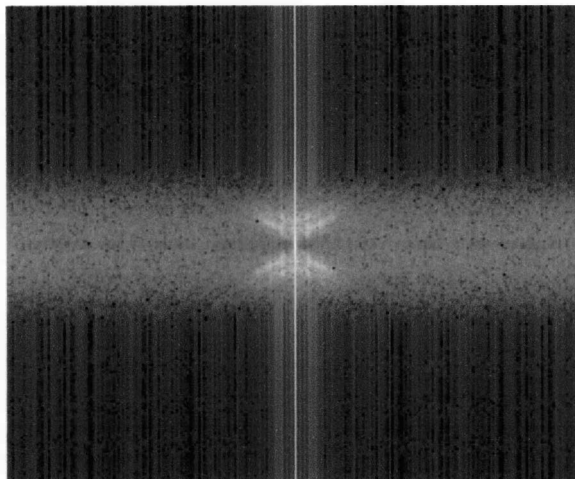


Figure 3-4: Fourier Transform of B-Scan of 4-Inch Slab

It is important to note that the diagonal arcs do provide information regarding the shape of the object and the dielectric constant of the surrounding medium. These arcs should be evaluated before being discarded. This method may fail when the dielectric constant of the medium changes or when delaminations add layers. Changes in the medium will alter the angle of the diagonal arcs both in the raw and Fourier transformed data. This may result in two or more sets of diagonals in the Fourier transformed data. Applying a broad filter may discard that information.

Automated Methods for Object Detection

Object detection methods from image processing have been applied to interpreting GPR scans, such as independent component analysis[17,24,27], neural networks and fuzzy logic[4,8,9,33], and ANOVA and other statistical methods[3,30,38]. These methods typically segment the data into regions, and measure the degree to which a region matches a template of an object. Regions with a high rating are declared to contain an object.

The template of simple objects has a clean mathematical definition. For instance, parallel horizontal layers produce horizontal lines and rebar produces hyperbolic arcs.[18,33] Other objects do not have such a clean definition, such as landmines.[10,26] Methods which detect irregularly shaped objects are usually statistical or neural algorithms which are trained with sample data.

Another field of research attempts to reconstruct the underground structure using back projection. These methods have have been used in seismology and are now being applied to GPR.[36]

Deconvolution

Both human and automated analysis of GPR scans begin with raw data. The model of GPR convolution shows that the data is a column-by-column convolution of the ground response with the transmitted pulse.

Humans intuitively deconvolve GPR data in the images. The expert looks for bands of light-dark-light or dark-light-dark in a B-scan, and declares the leading edge or

the center of the band to be “the line” of the reflection. The horizontal distance between these lines represents the time delay between pulses, and the amplitude of the center of the pulse represents the amplitude of the reflection.[28] This process is simple only for trivial cases. In real data, reflections overlap, obscuring the bands.

Automated methods can be constructed to detect objects within convolved data. The resulting system is tuned to data received from one specific transceiver and its specific pulse. An automated system must be completely retrained to process data from a different transceiver.

Deconvolution as a preprocessing step can solve these problems. Deconvolution describes methods for recovering the original ground response from the received data. The resulting image should be a series of clear lines and arcs. Deconvolution should increase the sharpness of the image for human evaluation and simplify the data for automated evaluation.[14]

Fourier Methods

A simple approach to deconvoluting GPR data is using the Fourier transform of the transmitted pulse and received signal to find the ground response.

$$R(f) = \frac{X(f)}{P(f)}$$

18

In practice, there will typically be frequencies where $P(f)$ is near zero and $X(f)$ is not. At those frequencies, $R(f)$ will be large. This can be remedied by using Weiner's Optimal filter, which adds a noise threshold c to the denominator.

$$R(f) = \frac{X(f)P^*(f)}{P(f)P^*(f) + c^2} \quad 19$$

This method is very fast and may create an image sharper than the original data. However, the peaks will tend to be broad and ringing will surround each peak. The results may be as indistinct as the original data.[25]

FIR Filter Methods

In theory, a finite impulse response filter $f(t)$ can be created such that

$$p(t) * f(t) \cong \delta(t) \quad 20$$

If this filter is applied to the received data, the result should be

$$s(t) * f(t) \cong r(t) \quad 21$$

This is a traditional approach in seismology and medical ultrasound[16,29,35]. There are many methods to constructing $f(t)$, including polynomial division with the Z-transform, construction of zero-phase filters by trial and error, and convolution as matrix multiplication.[21,37] These methods share the same strengths and weaknesses as the Fourier methods. The inversion of $p(t)$ tends to be badly formed and approaches infinity for some values, and remedies for this problem make the resulting peaks less sharp.

Blind Source Separation

Deconvolution can be approached as a blind source separation problem. Blind source separation begins with only the convolution of two signals, and uses the general statistical properties of the two original signals to recover the original signals.

Independent component analysis, Bussgang filters and other methods have been successful in deconvoluting GPR data.[2,20,29,32] These methods tend to be computationally expensive and are best used in situations where the initial pulse is unknown and unrepeatable, such as seismic data.

Optimization Methods

In general, optimization methods attempt to find a set of parameters $\{x_1, x_2, \dots, x_n\}$ that will minimize a rating function $F[\{x_1, x_2, \dots, x_n\}]$. In this application, $r(t)$ can be expressed as

$$r(t) \cong \sum_i a_i \delta(t - b_i) \quad 22$$

and the received signal $s(t)$

$$s(t) \cong \sum_i a_i p(t - b_i) \quad 23$$

The set of a_i 's and b_i 's becomes the parameter set. The rating function is the difference between the received signal and the current estimate

$$F[\{a_1, b_1, a_2, b_2, \dots, a_n, b_n\}] = \sum_t \left| s(t) - \sum_i a_i p(t - b_i) \right| \quad 24$$

There are a variety of 'off-the-shelf' algorithms for optimization such as Powell's Direction set method, downhill simples, anealing, and others.[31]

Optimization can be computationally expensive. Many optimization algorithms are sensitive to initial seed parameters. Some optimization algorithms depend on the derivatives of the rating function with respect to the parameters, which is not available in this case. Optimization algorithms may also be fooled by sub-optimal local minima.[21]

CHAPTER VI

OPTIMIZATION-BASED DECONVOLUTION AND SEGMENTATION ALGORITHM

The algorithm proposed in this thesis reduces the complexity of GPR scans by removing the transceiver's characteristic pulse from the GPR data. The first stage of the algorithm deconvolutes each column of the GPR data through an iterative decomposition method using correlation to locate the position of each target reflection. The second stage segments the deconvoluted image, converting it to a database of points and arcs. Objects matching chosen criteria can be highlighted, removed, or added to the final image. The final image is ready for human experts and for automated systems to evaluate.

Deconvolution

Iterative decomposition as a method for deconvolution has been proposed by other researchers. Kurtz et al (1997) proposed an iterative decomposition algorithm using derivative peak search and matched filter techniques to find pulses within GPR data[19]. Liu (1998) used iterative decomposition to find pulses in a subroutine[25]. Liu's subroutine performed its decomposition using a search grid of time and amplitude pairs. The grid had very large step size for the parameters resulting in very coarse results. These deliberately coarse results were then used as seed parameters for subsequent optimization algorithms.

The first stage of the proposed algorithm deconvolutes the GPR data column by

column. This deconvolution is through an optimization-based algorithm using iterative decomposition. Instead of optimizing the values of all parameters simultaneously, this method solves for a single parameter pair in each iteration. The time delays of each pulse are found using correlation.

Suppose that the goal was to find only the largest reflected pulse $p(t)$ contained within a GPR A-scan $s(t)$. This could be found by optimizing one parameter pair $\{a_1, b_1\}$. The algorithm would begin by finding the correlation between $p(t)$ and $s(t)$.

$$c(t) = \text{corr}[p(t), s(t)] \quad 25$$

The correlation time with the greatest absolute value would be assigned to b_1 . The algorithm would then vary a_1 over a range of values, and the value that minimizes $F[\{a_1, b_1\}]$ should be kept.

$$F[\{a_1, b_1\}] = \sum_t |s(t) - a_1 p(t - b_1)| \quad 26$$

The result should be the time delay and the amplitude of the largest echo of $p(t)$ found within $s(t)$. The ground response $r(t)$ of this single pulse is

$$r(t) = a_1 \delta(t - b_1) \quad 27$$

This pulse can be erased from the received signal, creating $s'(t)$

$$s'(t) = s(t) - p(t) * \delta(t) = s(t) - a_1 p(t - b_1) \quad 28$$

The updated signal $s'(t)$ may or may not have more pulses within it. It is apparent that this process may be repeated. That is the basic process of the proposed deconvolution algorithm: the most prominent pulse in the data is found and removed from the data, then the second-most, and so on until no more pulses can be detected.

The deconvolution algorithm is shown in flowchart form in Figure 4-1. The algorithm begins with all parameters set to zero. The transmitted pulse $p(t)$ and received GPR data $s(t)$ are inputs. The number of iterations is chosen to correspond to the number of spikes expected within $r(t)$. The algorithm begins by finding the correlation between the transmitted pulse and the received data with the previously detected pulses removed

$$c_i(t) = \text{corr} \left[p(t), s(t) - \sum_{j \neq i} s(t) - a_j p(t - b_j) \right] \quad 29$$

Note that all $\{a_j, b_j\}$ where $j < i$ have been discovered in prior iterations, and are treated as constants in the i^{th} iteration. All parameter pairs where $j > i$ are still initialized to zero. The time where the absolute value of $c_i(t)$ is a maximum is assigned to b_i . The algorithm varies a_i over a range of values to minimize the rating function

$$F[\{a_i, b_i\}] = \sum_t \left| s(t) - a_i p(t - b_i) - \sum_{j \neq i} a_j p(t - b_j) \right| \quad 30$$

If $F[\{a_i, b_i\}]$ is less than $F[\{a_{i-1}, b_{i-1}\}]$, the values of $\{a_i, b_i\}$ are kept. If $F[\{a_i, b_i\}]$ is not less than $F[\{a_{i-1}, b_{i-1}\}]$, or if its improvement is less than the threshold percentage, the values are rejected. The algorithm continues to the next iteration until the maximum number of iterations is reached or until the current parameter pair is rejected. At the end of the iterations, the ground response is

$$r(t) = \sum_{i=1}^I a_i \delta(t - b_i) \quad 31$$

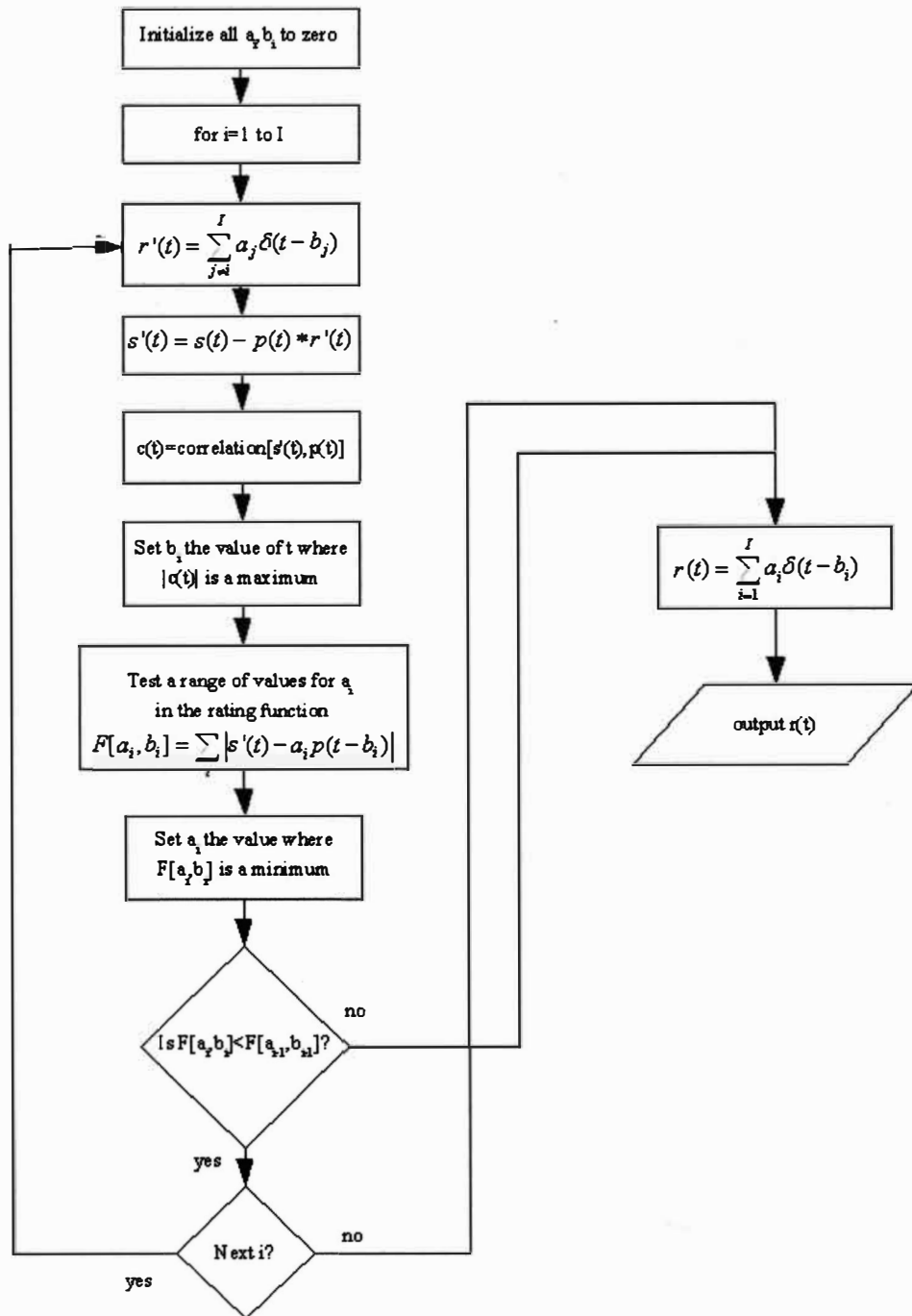


Figure 4-1: Flowchart of Deconvolution Algorithm

This method may produce errors due to false correlation and the overlapping of pulses. An example of this is shown in Figure 4-2. The upper plot shows a simulated ground response and the middle plot the simulated GPR scan. The lower plot shows the result of the deconvolution algorithm on the simulated GPR data. In the deconvoluted data, the large positive peaks are lower in amplitude and displaced slightly in time compared to the original. There are also smaller peaks that are not present in the original simulation.

This error appears consistently when pulses overlap at critical distances. The self interference creates noise in the correlation function, which leads to noise to the value of the chosen b_i . The algorithm then chooses a sub-optimal $\{a_i, b_i\}$ pair with small inaccuracies in time and amplitude. This sub-optimal choice in parameters will add error to the remainder $s'(t)$. This error will affect subsequent parameter pairs, typically leading to a series of low amplitude spikes in close proximity to the large, displaced spike.

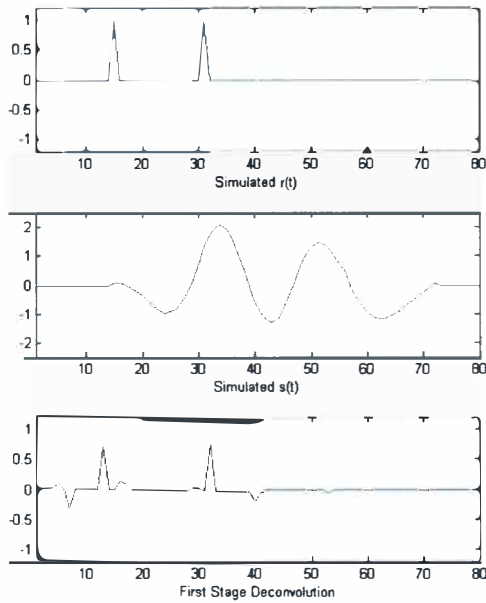


Figure 4-2: Deconvolution Error in a Simulated A-Scan

This error can be reduced with a sharpening algorithm similar to Powell's Direction set algorithm. In this algorithm, every parameter pair whose b_i is within a critical range of another pair's b_j and $|a_i| \ll |a_j|$ is reset to zero. The remaining nonzero parameters are varied one at a time over small intervals near their original values to minimize the rating function $F[a_i, b_i]$. The new parameter values should have greater amplitude than the original values, and the corresponding prominent spikes should be closer to their 'true' positions in time.

Figure 4-3 shows the results of the sharpening algorithm on the simulation. The upper image is a plot of the noisy deconvolution. The middle image shows the data with small noise surrounding the large spikes removed. The large spikes are still displaced in time and have incorrect amplitudes. The lower image shows the data after the remaining

spikes are varied and optimized. This result perfectly matches the original $r(t)$ shown in Figure 4-2. In practice, the improvement varies with the closeness of overlap and with the self-similarity of the pulse.

The flowchart of the sharpening algorithm is shown in Figure 4-4. This sharpening stage improves the accuracy of large, prominent spikes, but may discard valid low amplitude spikes. The first stage can be repeated to populate the zero value parameter pairs and recover weaker pulses.

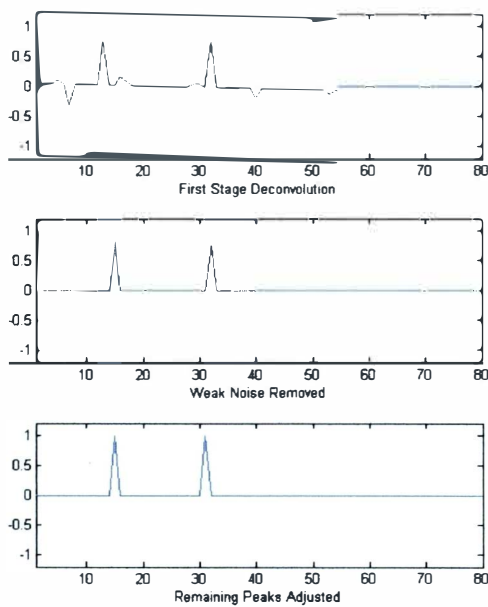


Figure 4-3: Correction of Deconvolution Error in a Simulated A-Scan

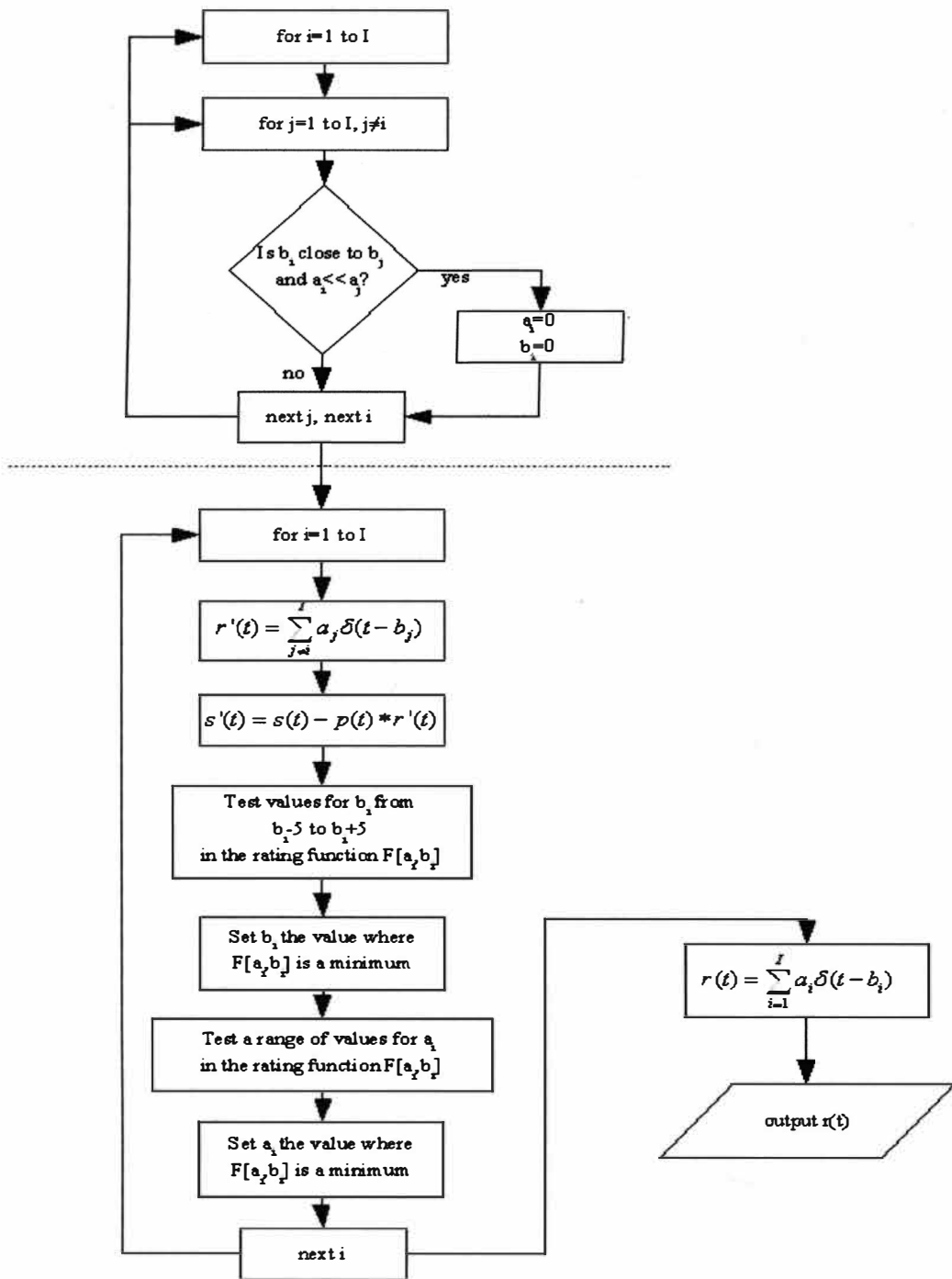


Figure 4-4: Flowchart of Sharpening Algorithm

Segmentation

The deconvolution algorithm is repeated for each column in the GPR data. The result should be a sparsely populated matrix with arcs of similarly valued cells. The second part of the proposed algorithm segments this new matrix.

The model of GPR predicts the amplitude of a reflected pulse depends primarily on the transmissions and reflections in its travel path. Suppose two GPR scans are taken at two distinct locations on a target and both pulses reflects off a single buried object. Assuming a simple structure, both reflected pulses will have the same reflections and transmission but different travel paths. The expected result is a pulse on each GPR scan with similar amplitudes and possibly different offset times. If several scans are taken with small changes in location, the reflections from the object will form a 'continuous' arc in the image of GPR data. Arcs will form for each reflection path.

These arcs appear also in the matrix of deconvoluted GPR data. Evaluation of this data may be aided by selectively removing some of these arcs. For instance, arcs with a extremely short width may be noise. Long arcs and lines may represent reflections from known objects, and can be removed to reveal more subtle reflections.

The algorithm scans downward from the top of the image, searching for a non-zero pixel not assigned to a group. When one is found, a new group is formed and it is assigned to the group. It then searches down and left for another non-zero pixel that is in close proximity, has a similar amplitude to the first, and is not assigned to a group. If such a pixel is found, it is assigned to the group and the search is repeated for the next nearby matching pixel down and left. This is continued until no more pixels matching

the criteria are found. The algorithm then returns to the starting pixel. A new group is formed, and the search is repeated the search down and right. When both paths are explored, the algorithm begins scanning for the next top pixel not assigned to a group, repeating the group creation and search process.

The segmenting process reformats the data from a matrix to a tabular format, like a database table or spreadsheet. This table would have columns for Group-ID, X, Y, and Pixel Amplitude. With the GPR data in tabular form, searches and queries can be performed on the groups. It is straightforward to find the length, the maximum and average amplitudes, and the highest point within each group. Group data can be used by automated systems to detect characteristic shapes formed by the X and Y coordinates of the group's pixels.

The GPR scan image can be easily rebuilt from the group table data. For each group to be included, each member pixel's amplitude is assigned to the (X,Y) coordinate in the new matrix. Groups can be included or excluded from the new image to remove noise and obvious features and to highlight details.

CHAPTER V

EXPERIMENTAL RESULTS

Simulation GPR Data

The deconvolution algorithm was tested on simulated GPR A-scans. The segmentation algorithm is only applicable to B-scans, so it was disabled for these tests. Figure 5-1 is a graph of the ground response of a simulated target, and Figure 5-2 the simulated GPR A-scan of that target. Figure 5-3 shows the results of the deconvolution algorithm on the A-scan data. Figure 5-4 is a reconstruction of the A-scan created by convoluting the transmitted pulse with the deconvoluted ground response. For ground responses whose spikes are separated by at least one quarter of the wavelength of the transmitted pulse, the deconvoluted ground response is extremely accurate.

The algorithm is also able to extract pulses from simulated scans with added noise with high accuracy. Figure 5-5 is the same simulated A-scan as in Figure 5-2 with white noise added with a SNR ratio of 2-1. Figure 5-6 shows the results of the algorithm deconvolving the noisy signal. Comparing Figure 5-6 with Figure 5-3, the added noise creates low amplitude spikes in the deconvoluted ground response. The contribution of these noise spikes is minimal in the reconstructed A-scan as seen in Figure 5-7. The noise filtering properties of the algorithm depend on the properties of the added noise. The lower the correlation between the noise and the transmitted pulse, the better the algorithm is at rejecting noise.

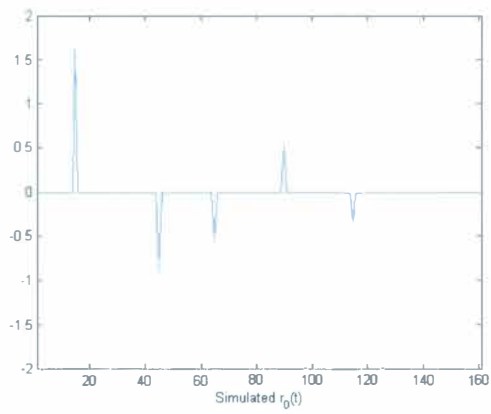


Figure 5-1: Simulated Ground Response

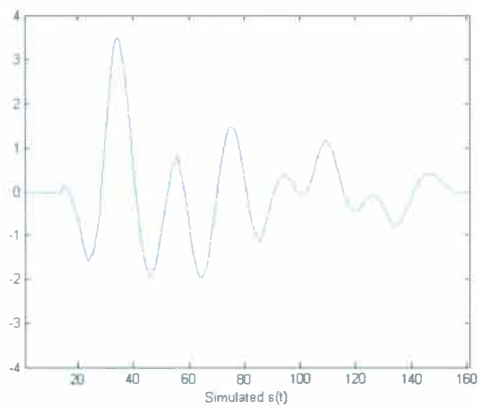


Figure 5-2: Simulated A-Scan

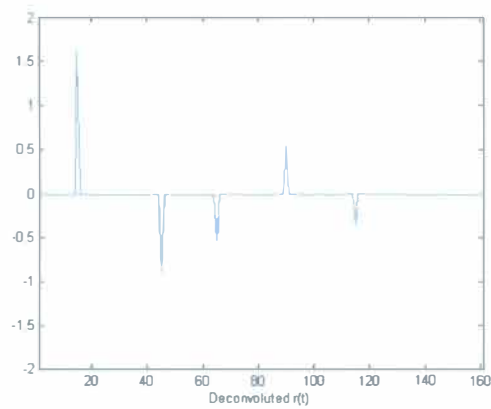


Figure 5-3: Deconvoluted Ground Response of A-Scan

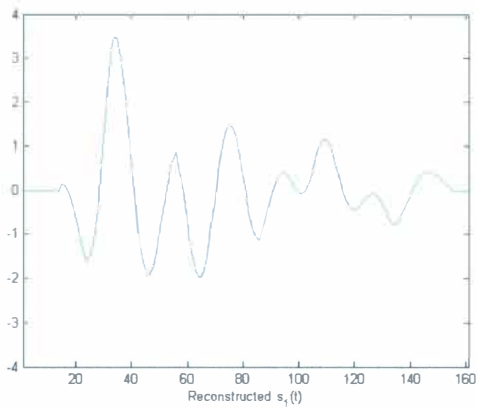


Figure 5-4: Reconstruction of A-Scan Using Deconvoluted Ground Response

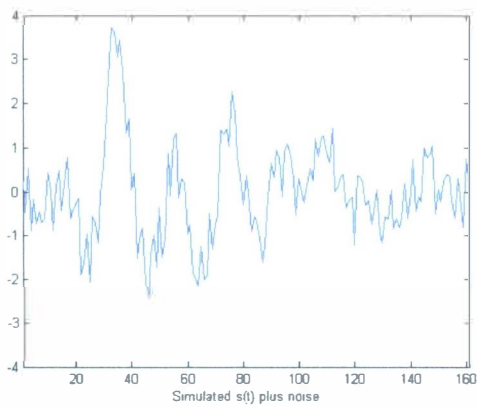


Figure 5-5: Simulated A-Scan with Added Noise

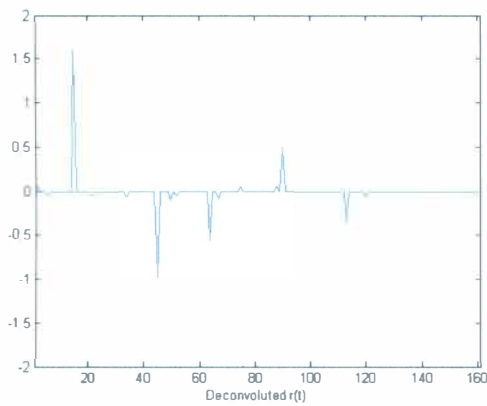


Figure 5-6: Deconvoluted Ground Response of A-Scan with Added Noise

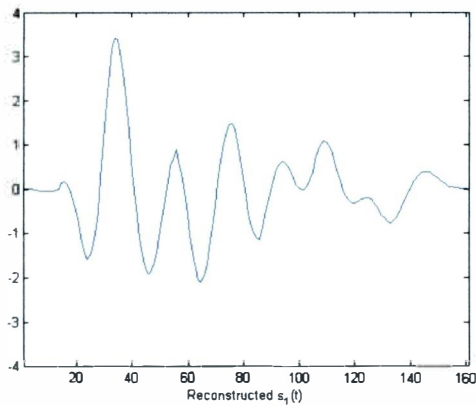


Figure 5-7: Reconstruction of Noise Free A-Scan Using Deconvoluted Ground Response

The deconvolution algorithm loses accuracy when prominent spikes in $r(t)$ are closer than one quarter the wavelength of the transmitted pulse. Figure 5-8 shows a simulated B-scan response made of two diagonal crossing lines, each with an amplitude of positive one. This simulation was convoluted against pulse $p(t)$, and deconvoluted by the algorithm. Figure 5-9 shows the deconvoluted response. The algorithm generates some noise when the pulses overlap about one half wavelength due to autocorrelation error. When the pulses are closer than one quarter wavelength, the algorithm merges the two pulses into a single pulse.

Figure 5-10 shows a simulated B-scan response made of two crossing lines with opposite polarities. This response was convoluted against pulse $p(t)$, and deconvoluted by the algorithm. Figure 5-11 shows the deconvoluted response. Again, the algorithm generates slight noise when the pulses overlap about one half wavelength. When the pulses are closer than one quarter wavelength, they cancel out leaving a blank region at the crossing.

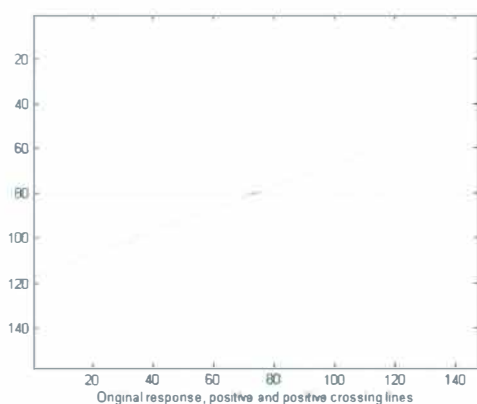


Figure 5-8: Simulated Ground Response of Crossing Lines with Same Polarity

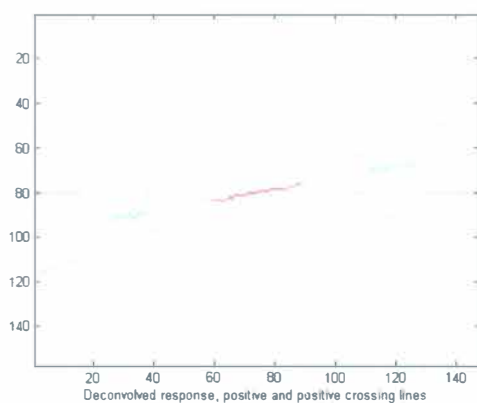


Figure 5-9: Deconvoluted Ground Response of Crossing Lines with Same Polarity

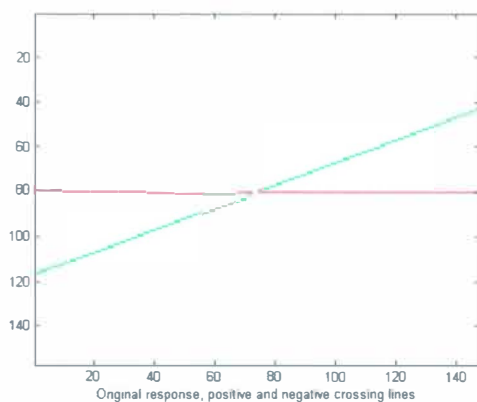


Figure 5-10: Simulated Ground Response of Crossing Lines with Opposite Polarity

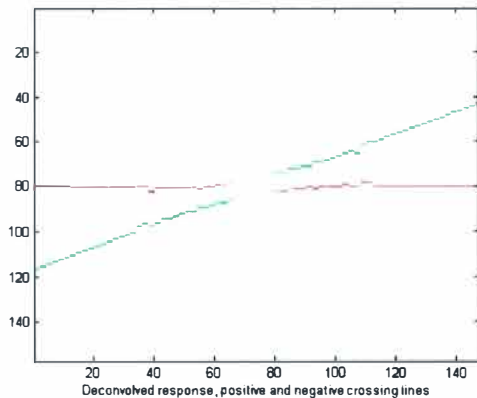


Figure 5-11: Deconvoluted Ground Response of Crossing Lines with Opposite Polarity

This error occurs because the deconvolution algorithm attempts to create a deconvolution using the fewest and highest amplitude spikes possible. If the algorithm did not seek to minimize the number of spikes, it would be prone to creating a large number of high amplitude spikes which cancel each other out. Minimizing the number of spikes is the good strategy for the algorithm to take, in the absence of additional information. Unfortunately the algorithm is vulnerable to local minima within the rating function $F\{a_i, b_i\}$, and may attempt to describe multiple spikes located closely together using one or zero spikes.

The deconvolution and segmentation algorithms were tested on simulated B-scans. Figure 5-12 shows a simulated ground response of a slab with rebar. Figure 5-13 shows the simulated B-scan of that slab. Figure 5-14 shows the result of applying the deconvolution algorithm to the simulated B-scan. Figure 5-15 shows the result of applying the segmentor algorithm to the deconvoluted results, and keeping arc segments with a length of five pixels or greater.

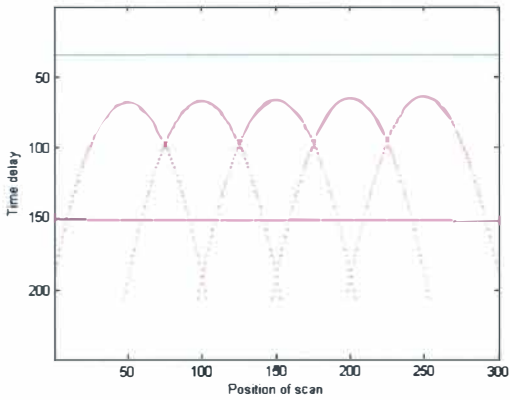


Figure 5-12: Simulated Ground Response of Concrete with Embedded Rebar

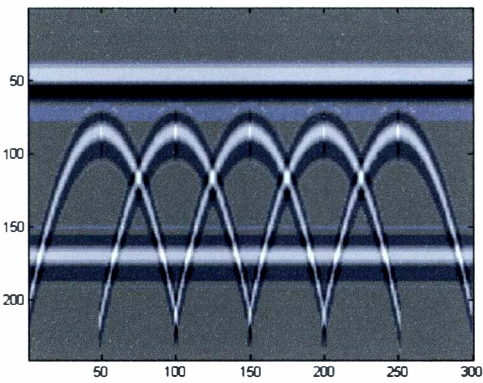


Figure 5-13: Simulated B-Scan of Concrete with Embedded Rebar

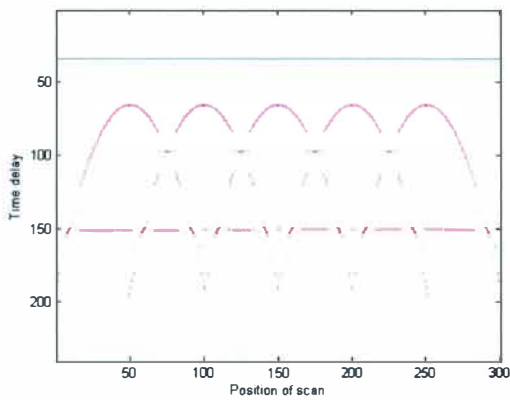


Figure 5-14: Deconvoluted Ground Response of Simulated B-Scan

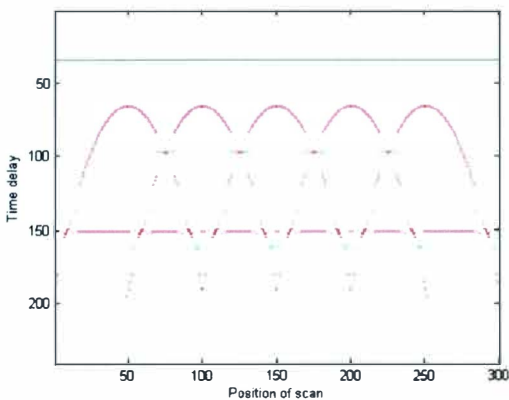


Figure 5-15: Deconvoluted and Segmented Ground Response of Simulated B-Scan

The deconvoluted result in Figure 5-14 matches the original response in Figure 5-12, with errors clustered near regions where arcs overlap. These error pixels tend to be lone pixels with low amplitude and no neighboring pixels. By rejecting all arcs below an average absolute amplitude or a specified length, as shown in Figure 5-15, the segmentor can remove most of the error pixels and leaves the main arcs intact. The data in Figures 5-14 and 5-15 is ready for use by a human evaluator or an automated object detection system.

Real GPR Data

Concrete test slabs have been created by WMU's Civil and Construction Engineering department.[28] These slabs were scanned using a Model 5100 antenna attached to an SIR System-2000 terminal, both from GSSI.[11] The data recorded from the scans was converted from GSSI's proprietary format to plain text, tab-delimited spreadsheets. The data was then processed using the deconvolution and segmentation algorithms. The deconvolution algorithm was applied to the data with an iteration

number of twenty. The deconvoluted data was segmented and reconstructed into a new image which excludes all arcs whose absolute average value is below a threshold.

Figure 5-16 is the GPR scan of a 4-inch test slab with embedded rebar. The slab has no defects. Figure 5-17 is the output of the deconvolution algorithm, and Figure 5-18 is the reconstructed data created by the segmentor algorithm.

The most prominent features in the GPR scan in Figure 5-16 are the horizontal line across the top and the seven arcs beneath it. The horizontal line represents the self-coupling, the signal transmitted directly from transmitter to receiver and the reflection from the air-concrete boundary. The seven arcs are hyperbolas, the signature shape of reflections off of the rebar within the concrete slab. One feature that is expected but not visible in this GPR scan are lower horizontal lines representing the concrete-wooden platform boundary and the rebar which are parallel to the direction of the scan. It is probable that these lines are obscured by the overlapping hyperbolas from the rebar.

The deconvoluted data in Figure 5-17 matches the original GPR scan. The faint horizontal line across the top of the image represents the self-coupling, and the bold line represents the first reflection off the air-concrete boundary. The seven arcs represent the upper portion of the hyperbolas. There is noise where the peak of each arc approaches the air-concrete reflection and where each arc crosses. Beneath four of the arc crossings are short line segments that may correspond to reflections from the concrete-wooden platform boundary. These segments are short and low amplitude; it is uncertain whether they are reflected signals or noise.

The segmented and filtered data in Figure 5-18 keeps the self-coupling and

ground lines and the seven arcs found in Figure 5-17 and removes some of the noise. It also removes many of the line segments which may be from the lower boundary. This demonstrates the risk in filtering the data; any criteria that rejects noise will also tend to reject faint signals as well.

Figure 5-19 is the GPR scan of a 6-inch test slab with embedded rebar. The slab has no defects. Figure 5-20 is the output of the deconvolution algorithm, and Figure 5-21 is the reconstructed data created by the segmentor algorithm. As with the 4-inch slab, the original data has a prominent self-coupling line and seven rebar hyperbolas. In the 6-inch slab, however, it is possible to see the reflection from the lower concrete-wooden platform boundary. This reflection is the horizontal line beneath the rebar peaks, and it is broken where the rebar arcs cross it.

The deconvoluted data in Figure 5-20 matches the original GPR scan. The two faint horizontal lines at the top of the image correspond to self-coupling, and the horizontal line to the first reflection from the air-concrete boundary. The arcs correspond to the upper portions of the hyperbolic arcs. The faint line segments below the arcs represents the reflection from the concrete-wooden-platform boundary. Because of the relative lack of noise in the deconvoluted data, the segmented and filtered data in Figure 5-21 is nearly identical to Figure 5-20.

Figure 5-20 demonstrates a short-coming of the deconvolution algorithm. In the original data in Figure 5-19, visual inspection shows that the hyperbolic arcs continue beyond the first arc crossing. The amplitude of the arcs in these lower regions is much less than at the peak. This is due to the exponential attenuation of the radar signal as it

passes through concrete. Humans can see these arcs because we extrapolate their presence; an observer sees the top of the arc, unconsciously predicts the continuation of the arc to the right and left of the peak, and finds faint signals within the noise that match the prediction. The deconvolution algorithm deconvoluted each column using only the information within that column. Because of this, the deconvolution algorithm treats the low amplitude arc segments below the arc crossings as noise and ignores them.

Figure 5-22 is the GPR scan of a 8-inch test slab with embedded rebar. The slab has no defects. Figure 5-23 is the output of the deconvolution algorithm, and Figure 5-24 is the reconstructed data created by the segmentor algorithm. The original data has a prominent self-coupling line, seven rebar hyperbolas, and a faint line from the lower boundary. The deconvoluted data has the self-coupling and ground-coupling lines, rebar arcs, and lower boundary line. For the 8-inch slab, the reflection from the concrete-wooden platform boundary is weak. The segmentation algorithm treats the lower boundary reflection as noise and rejects, as is shown in Figure 5-24. This can be prevented by changing the filter criteria.

A 4-inch test slab was constructed with embedded rebar and embedded defects. Small blocks of Styrofoam were embedded in the concrete to simulate delaminations and small plastic tubes were embedded to simulate voids. The layout of rebar and defects is shown in Figure 5-25. These defects should appear in a GPR scan as objects or as distortions of neighboring objects.

Figure 5-26 is the GPR scan of a 4-inch test slab with embedded rebar and defects. The slab has six rebar in the scanning region. Figure 5-27 is the output of the

deconvolution algorithm, and Figure 5-28 is the reconstructed data created by the segmentor algorithm. The data is similar to the scan of the 4-inch slab with no defects, shown in Figures 5-16, 5-17 and 5-18. The reflection from the lower concrete-wooden platform boundary is more visible in figure 5-27 than in Figure 5-17.

No new objects are visible between the ground coupling and the rebar peaks in the deconvoluted scan of the slab with defects. This actually is not surprising. It takes light .085 nanoseconds to travel one inch through air. Assuming the Styrofoam behaves like air with respect to light and that the embedded defect is one inch thick, the two-way travel time of light through the defect is .17 nanoseconds. The GPR takes a sample of the received signal every .028 nanoseconds. The time delay between the reflection from the upper concrete-defect boundary and the lower defect-concrete boundary will be .17 nanoseconds, a distance of six pixels in the GPR data. This interval is less than one quarter of the wavelength of the transmitted pulse, so it is too small an interval for the deconvolution algorithm to separate the two pulses. In addition, the concrete-defect boundary in this example is very close to the air-concrete boundary, and these pulses may be merged as well.

This does not make such a defect undetectable. The defect will also refract light, changing the path and travel time of the reflected pulse as it travels through the defect to and from objects beneath the defect. This results in a change in the shape of the reflected arcs and lines from objects beneath the defect. In Figure 5-27, the first four hyperbola are very similar in shape to the arcs found in the scans of defect-free slabs. The fifth and sixth arcs are deformed compared to the other arcs. They have distorted shapes, and they

do not appear to cross. This distortion raises suspicion of this region of the slab. The arrow in Figure 5-29 shows the actual path of the B-Scan shown in Figure 5-27, which includes two Styrofoam defects placed above two consecutive rebar. Therefore, the interpretation of this scan matches the defects present in the scan path.

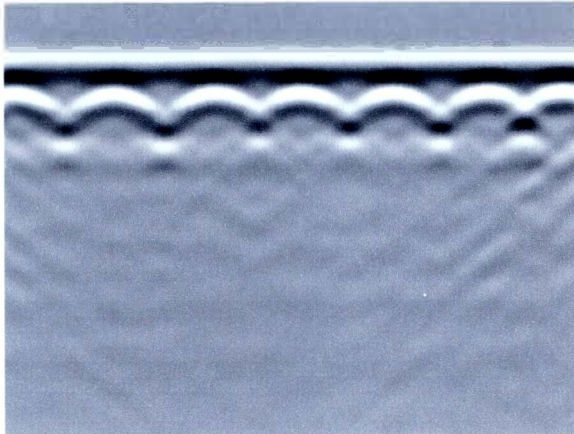


Figure 5-16: GPR Scan of 4-Inch Slab with No Defects

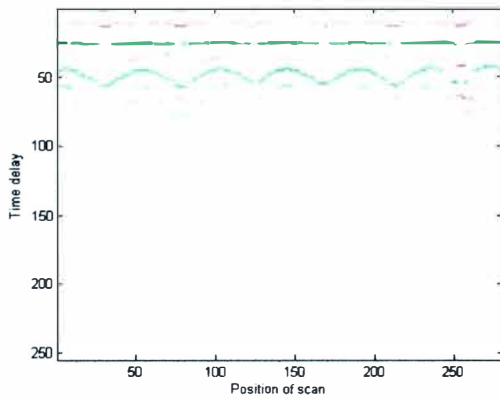


Figure 5-17: Deconvoluted Ground Response of 4-Inch Slab with No Defects

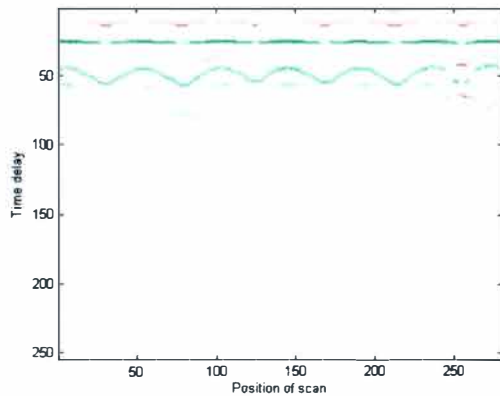


Figure 5-18: Deconvoluted and Segmented Ground Response of 4-Inch Slab with No Defects

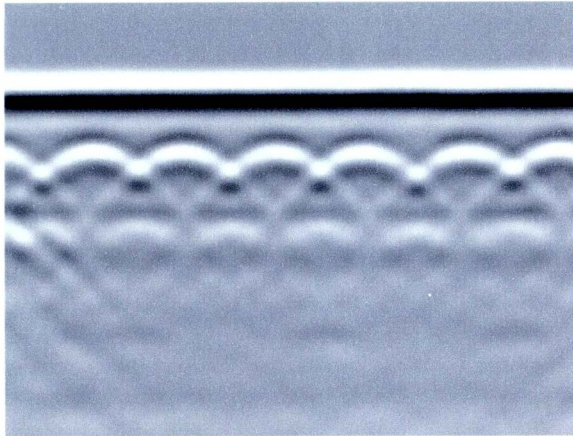


Figure 5-19: GPR Scan of 6-Inch Slab

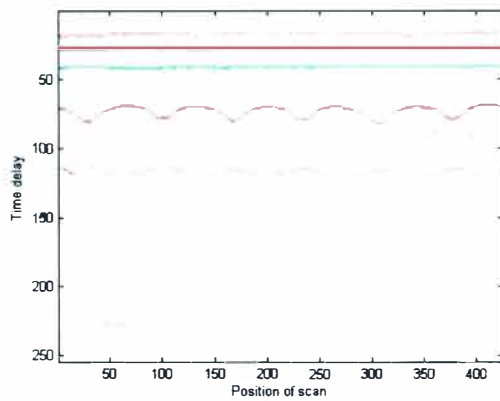


Figure 5-20: Deconvolution of GPR Scan of 6-Inch Slab

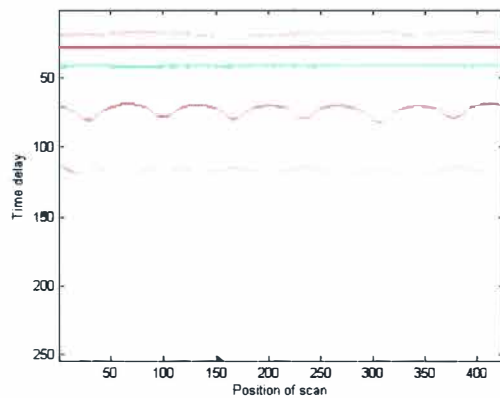


Figure 5-21: Deconvolution and Segmentation of GPR Scan of 6-Inch Slab

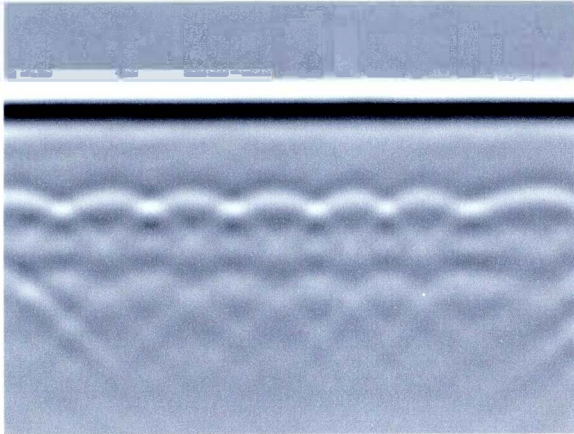


Figure 5-22: GPR Scan of 8-Inch Slab

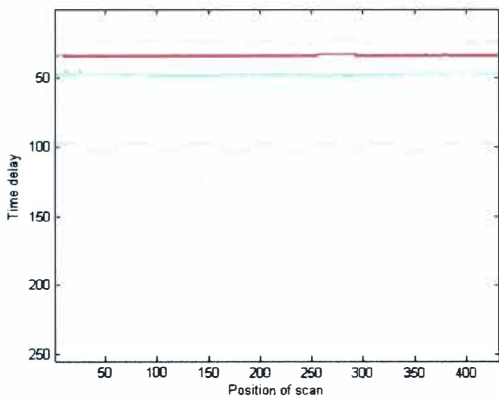


Figure 5-23: Deconvolution of GPR Scan of 8-Inch Slab

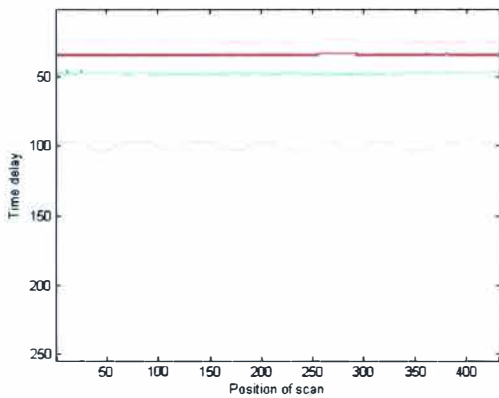


Figure 5-24: Deconvolution and Segmentation of GPR Scan of 8-Inch Slab

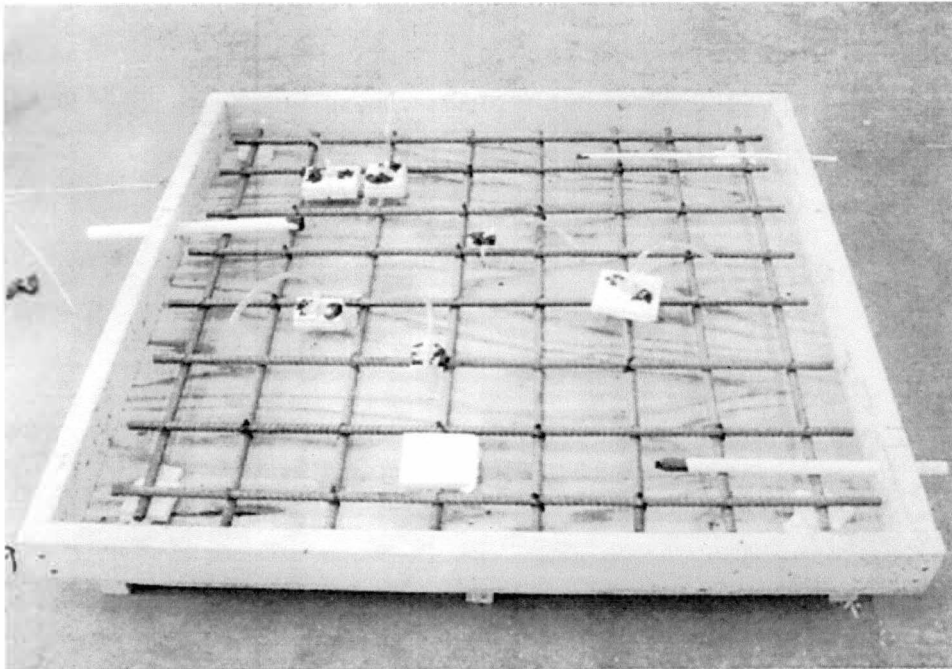


Figure 5-25: Construction of 4-Inch Slab with Embedded Defects

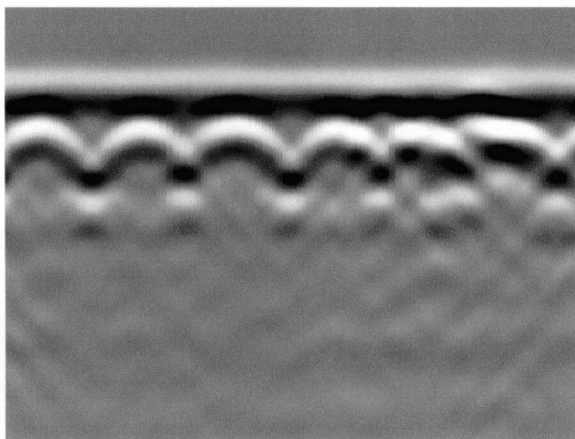


Figure 5-26: B-Scan of 4-Inch Slab with Embedded Defects

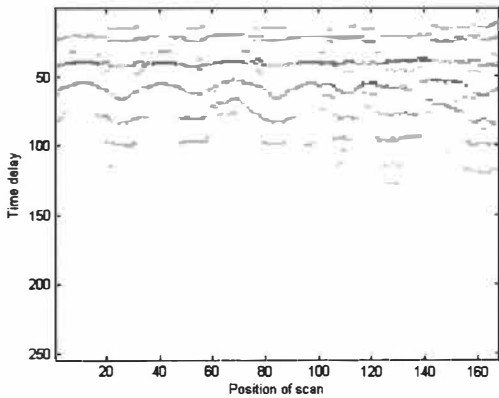


Figure 5-27: Deconvolution of GPR Scan of 4-Inch Slab with Embedded Defects

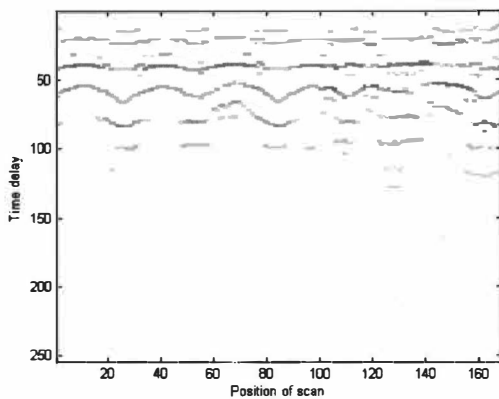


Figure 5-28: Deconvolution and Segmentation of GPR Scan of 4-Inch Slab with Embedded Defects

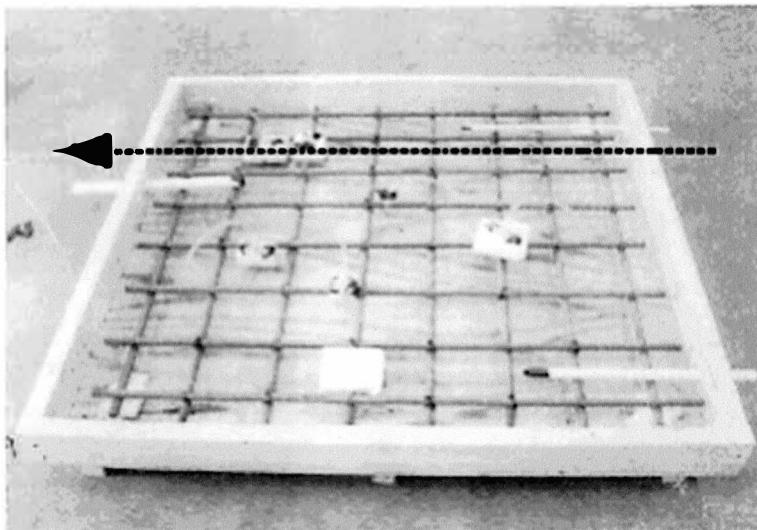


Figure 5-29: Actual Antenna Path of B-Scan

CHAPTER VI

CONCLUSION

This thesis proposed an algorithm for the deconvolution and segmentation of GPR scan data. The first stage algorithm treated deconvolution as an optimization problem, and using iterative decomposition to locate the position of each reflection spike. The second stage segmented the data, allowing the removal of features based on search criteria. The results of the algorithm were demonstrated using simulated and real GPR data.

The deconvolution algorithm was able to detect the prominent reflections in real GPR data, corresponding to the reflections from the top of the test slab and from rebar. The algorithm was able to detect the reflection from the bottom of the test slabs in some cases. It was able to clarify data from a scan of a slab with embedded defects well enough to allow the visual detection of the defects. The algorithm was unable to clarify arcs in regions with both low amplitude reflections and a high number of overlapping arcs. The segmentation algorithm was able to remove noise from the deconvoluted data by rejecting low amplitude arcs.

The proposed algorithm is intended to assist visual inspection of GPR data as well as serve as a preprocessing stage for object detection algorithms. When visually interpreting raw GPR data, faint reflections are hard to see. In the deconvoluted and segmented data, every arc can be displayed with any intensity or color scheme desired. The resulting image may allow road crews to evaluate roads and bridge decks using GPR

in less time, with less experience, and with less training.

Object detection methods are often trained using data gathered using a specific type of antenna. A drawback of this approach is that the method becomes dependent on that specific antenna type. For instance, an object detector designed to find rebar in bridge decks could not be used to detect pipes buried in soil. Even though the physics of these two situations are the same, the differences caused by the antennas designed for each situation would confuse the detector. The proposed algorithm removes these antenna characteristics from GPR data. The object detector can focus on the characteristic lines and arcs corresponding to underground objects.

Deconvoluting GPR data column by column is vulnerable to local minima within the rating function, and therefore to erroneous interpretations of the data. Future approaches may use the context provided by neighboring columns to improve the interpretation of the current column. One possible approach is to use an object detection algorithm to locate lines and hyperbolas within the segmented data. Ideal arcs could be plotted based on these detected arcs, and these ideal arcs used as seed values for a second round of deconvolution. This could clarify ambiguous interpretations in regions where reflections overlap.

BIBLIOGRAPHY

1. Annan, A. (1999) Practical Processing of GPR Data. Sensors and Software, Inc, Mississauga, ON, CA, 1999.
2. Bronstein, A., Bronstein, M, and Zibulevsky, M. (2005) Relative Optimization for Blind Deconvolution. *IEEE Transactions on Signal Processing*, vol 53, No 6, June 2005.
3. Brunzell, H. (1999) Detection of Shallowly Buried Objects Using Impulse Radar. *IEEE Transactions on Geoscience and Remote Sensing*, Vol 37, No 2, March 1999.
4. Caorsi, S. and Cevini, G. (2005) An Electromagnetic Approach Based on Neural Networks for the GPR Investigation of Buried Cylinders. *IEEE Geoscience and Remote Sensing Letters*, Vol 2, No 1, Jan. 2005.
5. Collings, L., Gao, P., and Carin, L. (1999) An Improved Bayesian Decision Theoretic Approach for Land Mine Detection. *IEEE Transactions on Geoscience and Remote Sensing*, Vol 37, No 2, March 1999.
6. Conyers, L. and Goodman, D. (1997) Ground Penetrating Radar: An Introduction for Archaeologists. AltaMira Press, Walnut Creek, CA.
7. Daniels, J. (2000) Ground Penetrating Radar Fundamentals. Prepared as an appendix to a report to the U.S. EPA, Region V, Nov. 25, 2000.
8. Delbo, S., Gamba, P., and Roccato, D. (2000) A Fuzzy Shell Clustering Approach to Recognize Hyperbolic Signatures in Subsurface Radar Images. *IEEE Transactions on Geoscience and Remote Sensing*, Vol 38, No 3, May 2000
9. Gamba, P. and Lossani, S. (2000) Neural Detection of Pipe Signatures in Ground Penetrating Radar Images. *IEEE Transactions on Geoscience and Remote Sensing*, Vol 38, No 2, March 2000.
10. Gelenbe, E. and Kocak, T. (2000) Area-Based Results for Mine Detection. *IEEE Transactions on Geoscience and Remote Sensing*, Vol 38, No 1, Jan 2000
11. Geophysical Survey Systems, Inc. (2006) GSSI Handbook for Radar Inspection of Concrete. Published by GSSI, Salem, NH.

12. Greenhalgh, S. and Marescot, L. (2006) Modeling and Migration of 2-D Georadar Data: A Stationary Phase Approach. *IEEE Transactions on Geoscience and Remote Sensing*, Vol 44, No 9, Sept. 2006.
13. Hauser, E. and Howell, M. (2001) Ground Penetrating Radar Survey to Evaluate Roadway Collapse in Northern Ohio. Symposium on Application of Geophysics to Environmental and Engineering Problems (SAGEEP) , Denver, Colorado, March 4-7, 2001.
14. Herman, H. (1997) Robotic Subsurface Mapping Using Ground Penetrating Radar. Doctor of Philosophy Thesis, Carnegie Mellon University, Pittsburgh, PN.
15. Huston, D., Fuhr, P., Maser, K., and Weedon, W. (2002) Nondestructive Testing of Reinforced Concrete Bridges using Radar Imaging Techniques. The New England Transportation Consortium Report 94-2.
16. Izzetoglu, M., Onaral, B, and Bilgutay, N. (2000) Wavelet Domain Least Squares Deconvolution for Ultrasonic Backscattered Signals, Proceedings fo the 22nd Annual EMBS International Conference, July 23-28, 2000
17. Karlsen, B., Sørensen, H., Larsen, J., and Jakobsen, K. (2003) . GPR Detection of Buried Symmetrically Shaped Mine-like Objects using Selective Independent Component Analysis. Proceedings of the 2003 Detection and Remediation Technologies for Mines and Mine-Like Targets, AeroSense 2003, vol. 5089, pp. 375-386, SPIE, 2003
18. Krause, V., Abdel-Qader, I., Abudayyeh, O., and Yehia, S. (2007) An Image Segmentation Algorithm for the Detection of Rebar in Bridge Decks from GPR Scans. *Electro/Information Technology Conference*, Chicago, IL, 2007.
19. Kurtz, J., Fisher, J., Skau, G., Armaghani, J, and Moxley, J. (1997) Advances in Ground Penetrating Radar for Road Subsurface Measurements. *Proceedings of SPIE*, vol 3066, June 1997.
20. Larue, A., Mars, J., and Jutten, C. (2006) Frequency-Domain Blind Deconvolution Based on Mutual Information Rate. *IEEE Transactions On Signal Processing*, Vol. 54, No. 5, May 2006
21. Lahouar, S. (2003) Development of Data Analysis Algorithms for Interpretation of Ground Penetrating Radar Data. Doctor of Philosophy thesis, Virginia Polytechnic Institute and State University.
22. Lee, J. S., Nguyen, C. and Scullion, T. (2004) A Novel, Compact, Low-Cost Impulse Ground Penetrating Radar for Nondestructive Evaluation of Pavements.

23. Lewis, J., Owen, W., and Narwold, C. (2002) GPR as a Tool for Detecting Problems in Highway Related Construction. 2nd International Conference on the Application of Geophysical and NDT Methodologies to Transportation Facilities and Infrastructure, Los Angeles, CA, May 15-19, 2002.
24. Liu, J.-X., Zhang, B. and Wu, R.-B. (2006) GPR Ground Bounce Removal Methods Based on Blind Source Separation. Progress in Electromagnetics Research Symposium, Cambridge, MA, USA, March 26-29, 2006.
25. Liu, R. (1998) Deconvolution of Ground Penetrating Radar Signals for Condition Assessment of Bridge Decks and Pavements. Master of Science thesis, West Virginia University.
26. Miller, E., Kilmer, M., and Rappaport, C. (2000) A New Shape-Based Method for Object Localization and Characterization from Scattered Field Data. IEEE Transactions on Geoscience and Remote Sensing, Vol 38, No 4, July 2000.
27. Morgenstjerne, A., Karlsen, B., Larsen, J., Sorensen, H., and Jakobsen, K. (2005) A Combined Study of EMIS and GPR Detectors by the Use of Independent Component Analysis. NDRF Summer Conference, Aug. 24-26, 2005.
28. Nabulsi, S. (2005) The Detection of Common Concrete Bridge Deck Defects Using Thermography, Impact Echo, and Ground Penetrating Radar. Master of Science thesis, Western Michigan University.
29. Nsiri, B., Boucher, J. M., and Chonavel, T. (2003) Multichannel Blind Deconvolution Application to Marine Seismic. OCEANS 2003. Proceedings, Volume 5, Sept. 22-26, 2003.
30. Potin, D., Duflos, E., and Vanheeghe, P. (2006) Landmines Ground Penetrating Radar Signal Enhancement by Digital Filtering. IEEE Transactions on Geoscience and Remote Sensing, Vol 44, No 9, Sept. 2006.
31. Press, W., Teukolsky, S., Vetterling, W. and Flannery, B. (1992) Numerical Recipes in C: The art of Scientific Computing, Second Edition. Cambridge University Press, Cambridge, England.
32. Santamaria, I., Pantaleon, C., Ibanez, J. and Artes, A. (1999) Deconvolution of Seismic Data Using Adaptive Gaussian Mixtures. IEEE Transactions on Geoscience and Remote Sensing, Vol 37, No 2, March 1999.
33. Shaw, M., Millard, S., Molyneaux, T., Hungey, J., and Taylor, M. (2003) Location

of Steel Reinforcement In Concrete Using Ground Penetrating Radar and Neural Networks. Engineering Technics Press, London, 2003.

34. Song, J, Liu, Q. H., Torrione, P. and Collins, L. (2006) Two-Dimensional and Three-Dimensional NUFFT Migration Method for Landmine Detection Using Ground Penetrating Radar. *IEEE Transactions on Geoscience and Remote Sensing*, Vol 44, No 6, Jun 2006.
35. Titchkosky, K., (1968) Seismic Deconvolution. Self-published course notes, University of Toronto.
36. Wu, Z. and Liu, C. (1999) An Image Reconstruction Method Using GPR Data. *IEEE Transactions on Geoscience and Remote Sensing*, Vol 37, No 1, Jan. 1999.
37. Xia, J., Weis, T., Franseen, E., and Miller, R. (2001) Deterministic Deconvolution of Ground Penetrating Radar Data at a Limestone Quarry. Symposium on Application of Geophysics to Environmental and Engineering Problems (SAGEEP) , Denver, Colorado, March 4-7, 2001.
38. Xu, X., Miller, E., Rappaport, C., and Sower, G. (2002) Statistical Method to Detect Subsurface Objects Using Array Ground Penetrating Radar Data. *IEEE Transactions on Geoscience and Remote Sensing*, Volume 40, Issue 4, Apr 2002.